nature structural & molecular biology

Article

https://doi.org/10.1038/s41594-024-01367-7

The cyanobacterial protein VIPP1 forms ESCRT-III-like structures on lipid bilayers

Received: 5 October 2023

Accepted: 3 July 2024

Published online: 26 July 2024



Sichen Pan¹, Karin Gries², Benjamin D. Engel ®³, Michael Schroda ®², Christoph A. Haselwandter ® 4.5 & Simon Scheuring ® 1.6 ⊠

The biogenesis and maintenance of thylakoid membranes require vesicle-inducing protein in plastids 1 (VIPP1). VIPP1 is a member of the endosomal sorting complex required for transport-III (ESCRT-III) superfamily, whose members form diverse filament-based supramolecular structures that facilitate membrane deformation and fission. VIPP1 cryo-electron microscopy (EM) structures in solution revealed helical rods and baskets of stacked rings, with amphipathic membrane-binding domains in the lumen. However, how VIPP1 interacts with membranes remains largely unknown. Here, using high-speed atomic force microscopy (HS-AFM), we show that VIPP1 assembles into right-handed chiral spirals and regular polygons on supported lipid bilayers via ESCRT-III-like filament assembly and dynamics. VIPP1 filaments grow clockwise into spirals through polymerization at a ring-shaped central polymerization hub, and into polygons through clockwise polymerization at the sector peripheries. Interestingly, VIPP1 initially forms Archimedean spirals, which upon maturation transform into logarithmic spirals through lateral annealing of strands to the outermore low-curvature spiral turns.

Oxygenic photosynthesis in cyanobacteria and chloroplasts is performed by photosynthetic complexes embedded in thylakoid membranes. In cyanobacteria, the thylakoid membrane is also the major site of electron transport in respiration¹. Thylakoid membrane biogenesis and maintenance require VIPP1 (refs. 2-4), also known as the inner membrane associated protein of 30 kDa (IM30). VIPP1 localizes to the cytoplasm in cyanobacteria^{5,6} or the stroma in chloroplasts^{7,8}, and is associated with thylakoid membranes as well as plasma membranes in cyanobacteria^{5,6,9} or inner envelopes in chloroplasts^{2,3}. Disruption of VIPP1 results in reduced thylakoid formation in Synechocystis^{4,10,11}, Chlamydomonas⁷ and Arabidopsis^{3,12,13}, which is primarily attributed to the absence of VIPP1-dependent lipid transport to thylakoids^{3,14}. In addition, VIPP1 responds to cellular stress to protect thylakoids or chloroplasts from swelling, presumably by maintaining membrane integrity^{7,8,13,14}. In accordance, live-cell fluorescence imaging of Synechocystis has demonstrated that diffusing VIPP1 assembles into punctae at high-curvature regions of thylakoids near the cell periphery upon transitioning from low-light to high-light exposure, whereas perturbation of VIPP1 localization causes severe growth defects^{6,9}.

When interacting with membranes, VIPP1 can self-assemble into higher-order complexes, which are observed as irregular structures 13 , localized punctae 6,8,9 and tubules 14 in vivo, and as rings $^{5,14-17}$, rods 18 , filaments 17 and baskets $^{15-18}$ in vitro. However, the disassembly of higher-order complexes seems to be required to activate the membrane protection and fusion function of VIPP1 (refs. 16,19-22).

ESCRT is crucial to various membrane-remodeling processes, such as membrane repair and maintenance, vesicle and viral budding and cytokinetic abscission, in which ESCRT-III proteins are the core components^{23,24}. Recent studies using phylogenetic analysis and cryo-EM have reported that VIPP1 and its bacterial homolog PspA are ESCRT-III superfamily members and adopt an open conformation in supramolecular ring and rod structures^{14,17,25}. Importantly, the open

¹Weill Cornell Medicine, Department of Anesthesiology, New York, NY, USA. ²Molecular Biotechnology and Systems Biology, RPTU Kaiserslautern-Landau, Kaiserslautern, Germany. ³Biozentrum, University of Basel, Basel, Switzerland. ⁴Department of Physics and Astronomy, University of Southern California, Los Angeles, CA, USA. ⁵Department of Quantitative and Computational Biology, University of Southern California, Los Angeles, CA, USA. ⁶Weill Cornell Medicine, Department of Physiology and Biophysics, New York, NY, USA. ⊠e-mail: sis2019@med.cornell.edu

conformation is adopted by most ESCRT-III subunits in polymers and activates ESCRT-III to form membrane-remodeling supramolecular structures such as filaments, spirals and helical tubes^{26–30}.

Intriguingly, archaeal and eukaryotic ESCRT-III supramolecular structures are formed by mono- or multi-component filaments³¹. For instance, Snf7 has been observed to form single- or double-stranded homofilaments³²⁻³⁴, in which the carboxy terminus of each subunit restricts the lateral association of filaments and therefore inhibits membrane bud formation 32,35. Likewise, the formation of multi-component filaments has also been observed for CHMP1B-IST1, Snf7-Vps24 and CHMP2A-CHMP3. In these cases, electrostatic interactions drive the lateral association between strands^{29,36,37}. On the basis of these observations, a sequential polymerization and subunit-turnover model of ESCRT-III proteins has been proposed for membrane remodeling 38,39. First, ESCRT-III components are recruited sequentially to form hetero-filaments. Then, subunits are removed by the AAA-ATPase Vps4, leading to a turnover of components with different preferred curvature and rigidity, which would facilitate the shape transition of supramolecular structures. This process, also termed the spiral spring model³³, eventually proceeds towards membrane abscission^{30,37-40}.

Although the polymerization mechanism and dynamics of ESCRT-III have been extensively studied, it is unknown how the newly identified ESCRT-III homolog VIPP1 assembles on membranes at the molecular and supramolecular scales. In addition, a notable difference between bacterial and chloroplast VIPP1 and the eukaryotic ESCRT-III system is that the bacterial/chloroplast system consists of only one known ESCRT-III protein⁴¹, which calls for a different mechanism of assembly maturation and constriction that does not rely on exchanging multi-component subunits.

Here, we used HS-AFM to quantitatively study the polymerization process of VIPP1 on supported lipid bilayers (SLBs). We find that VIPP1 polymerizes spontaneously on negatively charged membranes into ESCRT-III-like filaments that form right-handed spirals and regular polygons. Notably, spirals are formed through protomer association to a ring-shaped central polymerization hub and an outward 'flow' of filament. In the later stages of spiral maturation, outward turns with lower curvature anneal subunits and thicken, leading to a transformation from an Archimedean to a logarithmic spiral. By contrast, polygons polymerize through peripherally growing filaments. Thus, the polymerization processes and kinetics of spiral and polygonal supramolecular structures are different, and our HS-AFM experiments also show that large enough spirals can transform into regular polygons. We hypothesize that lateral association of VIPP1 subunits to the filaments, that is, filament thickening, could represent a mechanism to modulate polymer mechanics as the supramolecular structures mature.

Results

VIPP1 polymerizes into spirals and polygons on membranes

To study VIPP1 polymerization on membranes, we used HS-AFM to observe the growth process of VIPP1 structures on SLBs. The SLBs were formed by physisorption and spreading of small unilamellar vesicles (SUVs) composed of 50% 1,2-dioleoyl-sn-glycero-3-phosphocholine (DOPC) and 50% 1,2-dioleoyl-sn-glycero-3-phospho-L-serine (DOPS) on the mica surface. Subsequent to SLB formation, VIPP1 was added into the fluid chamber to a final concentration of $2 \mu M$ (Fig. 1a). To verify SLB formation on mica, we imaged SUV spreading in absence of VIPP1 until the mica surface was entirely covered by a SLB (Fig. 1b).

First, we acquired HS-AFM videos of a 7 μ m \times 7 μ m overview of VIPP1 polymerization on membranes. After nucleating on the membrane, VIPP1 polymerized into filaments, which then formed supramolecular structures until the entire membrane was covered after ~30 min (Fig. 1c and Supplementary Video 1). Notably, two major supramolecular structures were detected (Fig. 1d,e): spirals and polygons, in contrast to other ESCRT-III proteins that form exclusively spirals on SLBs 27,33,34,38,39,42 . Polygons had a regular shape during their growth and

featured intersector grain boundaries from the center to the vertices. Polygons grew uniformly until other polymers perturbed their growth sterically (Fig. 1d). Nascent VIPP1 spirals grew rapidly and exhibited visible rotation during growth, and the thickness of their spiral turns increased gradually towards the periphery (Fig. 1e). For VIPP1 polymerization to occur, approximately 50% of the lipids in the SLB had to be negatively charged DOPS. In addition, we found that, with higher DOPS content, DOPS increased nucleation, but VIPP1 patches were smaller (Extended Data Fig. 1).

To assess the morphology and dynamics of VIPP1 growth in the HS-AFM videos statistically, we classified isolated VIPP1 polymers only, that is, individual VIPP1 structures that grew without environmental perturbations (n = 46, Fig. 1f and Supplementary Video 2). Our statistical analysis first showed that VIPP1 polymers exhibited two typical structures, spirals (67%) and polygons (20%). VIPP1 also formed mixed spiral—polygon structures (13%), which had a center composed of a spiral and a polygonal periphery. Second, we observed only chiral right-handed spirals, whereas all polygons were achiral. Third, most spirals and all polygons appeared static during growth, but 29% of spirals displayed rotation of their distal end, and they all rotated clockwise (CW). Thus, the spirals had conserved chirality and growth rotation. Left-handed spirals could be found occasionally as a final state, but only in crowded environments in which the favorable growth direction was blocked by other assemblies (Supplementary Video 3).

We analyzed the details of VIPP1 polymerization, beginning at the nucleation of each individual assembly. By measuring the time interval between starting points for growth of individual VIPP1 assemblies, we calculated the cumulative density function of VIPP1 nucleation time (Fig. 1g), yielding a characteristic time constant of ~2.8 min, which corresponds to a nucleation rate of 0.007 μm^{-2} min $^{-1}$.

We thus wondered what the typical oligomeric state of VIPP1 was in solution before nucleation and polymerization on the membrane. To this end, we performed mass photometry (Extended Data Fig. 2) and analyzed particle size in solutions containing either protein-free buffer or samples equilibrated at 0.6 μM or 2 μM VIPP1 bulk concentration (Fig. 1h). The mass photometry measurements peaked at ≤ 60 kDa in both concentrations. Because mass photometry measurements have a lower detection limit of -40 kDa (refs. 43,44), we concluded that at a 2 μM concentration, VIPP1 existed mainly as monomers or dimers in solution, which polymerized directly into spirals and polygons on membranes.

Next, we analyzed the height of VIPP1 polymer assemblies above the bilayer without selecting for a specific morphology. This analysis revealed a height of 7.2 ± 1.1 nm above the membrane (mean \pm s.e.m., Fig. 1i), in good agreement with the ~7-nm thickness of the protein density of VIPP1 rings around enclosed bilayers in situ¹⁴. Therefore, we propose that the VIPP1 assemblies on the SLBs are mono-molecular layers.

Finally, we analyzed the surface coverage of the total VIPP1 assembled area as a function of time (Fig. 1j). This analysis showed that the total coverage versus time trace had a sigmoidal shape, likely emerging from the time lag of nucleation, the average growth characteristics of the assemblies and a slowdown of growth due to steric clashes between assemblies. Thus we found a characteristic time for VIPP1 membrane coverage (μ) of ~14 min, and the average polymerization rate was ~3.4 μ m² min¹ at 2 μ M VIPP1. As expected, the polymerization rate increased as bulk concentration increased (Extended Data Fig. 1).

Altogether, at a low concentration of $\leq 2~\mu$ M, VIPP1 is predominantly monomeric, or of low oligomeric state, in solution and adsorbs to a negatively charged SLB with a nucleation rate of -0.007 μ m⁻² min⁻¹. Upon nucleation, VIPP1 forms spirals, polygons and mixed spiral–polygon assemblies. The spirals are reminiscent of those formed by ESCRT-III and have conserved right-handed architecture. The spiral polymerization process is also conserved and seems to occur in the spiral center; the peripheral ends of the observed spirals are of constant length and structure, and exhibit CW rotation as

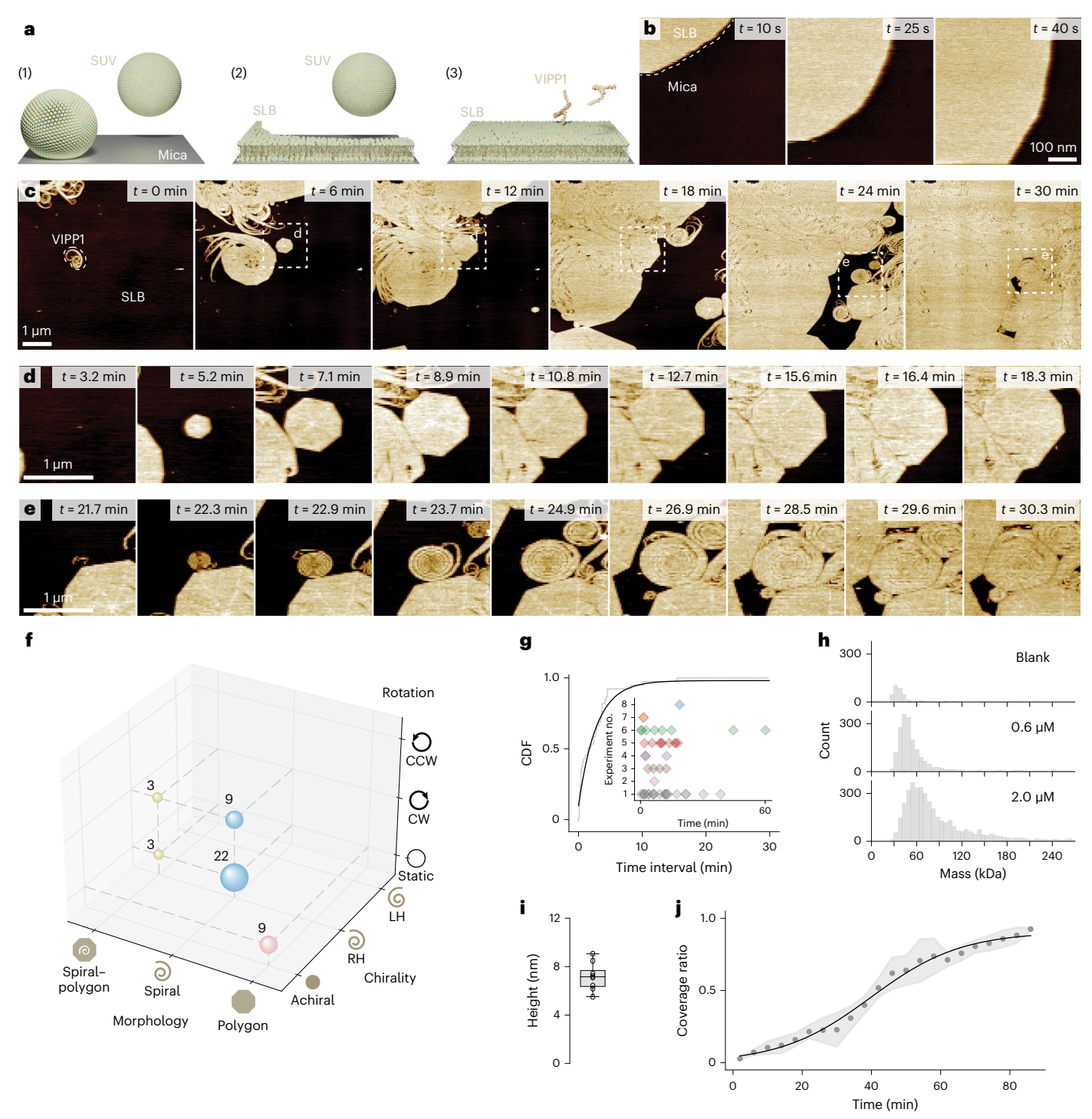


Fig. 1 | VIPP1 polymerization into spirals and polygons on SLBs. a, Schematic of the HS-AFM experiment for studying VIPP1 on membranes. (1) SUVs are incubated on freshly cleaved mica. (2) SUVs burst and spread on the mica surface to form a continuous SLB. (3) The SLB is immersed into the HS-AFM fluid chamber containing VIPP1, which polymerizes on the SLB. **b**, HS-AFM imaging of SLB formation on mica through SUV spreading. **c**, HS-AFM images of VIPP1 polymerization on SLB (Supplementary Video 1). The regions enclosed by dashed squares are enlarged in **d** and **e**, as indicated in the figure. **d**, VIPP1 polygon growth. **e**, VIPP1 spiral growth. **f**, Classification of VIPP1 polymer morphology. Number and sphere size indicate the count in corresponding classes (RH, righthanded; LH, left-handed; CW, clockwise; CCW, counter-clockwise). **g**, Cumulative

density function (CDF) of VIPP1 nucleation, that is, the time until polymerization, fitted by a one-exponential decay model. Inset, time points of events from eight biologically independent experiments. **h**, Mass photometry histograms of particles at equilibrated concentrations of 0 μ M, 0.6 μ M and 2.0 μ M VIPP1. VIPP1 is monomeric, or of low oligomeric state, in solution. **i**, Average VIPP1 assembly height (7.2 \pm 1.1 nm) above the SLB (all morphologies, mean \pm s.e.m, n = 8). Box, first (Q1) to third (Q3) quartile; circles, mean values; line, median value. Top whisker, Q3 + 1.5 \times interquartile range (IQR); bottom whisker, Q1 – 1.5 \times IQR. **j**, Surface coverage ratio as a function of time. The data points are presented as mean values and were fitted by a logistic model (black line, Methods). Light gray region, s.d. (n = 8, Supplementary Video 1).

the spiral radius increases. The shapes of polygons are regular, and these structures show peripheral growth. Spirals and polygons are mono-molecular layers of VIPP1. Once nucleation occurs, the growth process is fast, with a growth rate of ~3.4 $\mu m^2 \, min^{-1}$. To obtain a more detailed understanding, we next analyzed VIPP1 spirals and polygons at the single-assembly level.

VIPP1 forms spirals of flexible filaments

To elucidate VIPP1 spiral morphology, we analyzed HS-AFM images of VIPP1 spirals under equilibrium conditions, in which high spatial resolution could be achieved on static assemblies. VIPP1 polymerized into spirals with varying filament thickness, a constant height and a more strongly protruding ring at the center (Fig. 2a and Supplementary Video 4). Given that the height of the filaments was rather constant. corresponding to a mono-molecular layer of VIPP1, the varying filament thickness must represent lateral association of several VIPP1 subunits⁴⁵. The filament protrusion height ranged from 7 nm to 9 nm. Spiral filaments had an approximately constant height of 7 nm; the highly curved ring-shaped structures in the center of the assemblies were substantially taller, with a height of up to 9 nm (Fig. 2b). The subunits in high-curvature filaments could have a different conformation than those in the filaments at a larger spiral radius, or these rings could represent intercalated rings with stacked subunits, resembling the first two or three rings in the baskets imaged by cryo-EM14,17 (Extended Data Fig. 3).

Although the spiral center was confined to a small region by surrounding filaments, the tails of isolated spirals were flexible and fluctuated freely (Fig. 2c,d and Supplementary Video 5). Using these fluctuations, we calculated the filament persistence length³³, which ranged from ~200 nm at ~20-nm filament thickness to ~1.5 µm at ~60-nm filament thickness. Compared with the persistence length of actin, ~17 µm, and that of microtubules, ~1 mm (ref. 46), the VIPP1 filament is flexible even at increased thickness. We estimated the filament elasticity by fitting the individual tails' persistence lengths using the elastic rod model, yielding a lateral Young's modulus of ~34 kPa (Fig. 2e). Although an individual VIPP1 subunit in ring-stacked baskets interacts with up to 16 neighboring subunits¹⁴, mono-molecular filaments, potentially laterally annealed to form filaments of varying thickness, are flexible and can accommodate a wide range of curvatures⁴⁵. Similar to the inter-filament branching that has been observed in Snf7 spirals³³, dissociation and reassociation of adjacent filaments within spirals were also observed in VIPP1 and could also occur dynamically in the tails, which potentially contributes to the observed variability in the physical properties of filaments (Extended Data Fig. 3 and Supplementary Video 6).

High-resolution HS-AFM images revealed several architectural characteristics found in spirals (Fig. 2f and Supplementary Video 7). First, there is a ring-shaped structure at the spiral center, that is the nucleation and polymerization hub. Second, the thickness of filaments increased with increasing spiral radius. Indeed, the spiral filament could be fitted by a logarithmic spiral model (Extended Data Fig. 3). Third, the thicker filaments consisted of laterally aligned VIPP1 subunits. The resolution of VIPP1 subunits in these images resulted in a halo in two-dimensional (2D) power spectrum, indicative of a ~4.8-nm periodicity (Fig. 2g). Intriguingly, filaments formed flat patches occasionally (Fig. 2f, bottom right, and Supplementary Video 7). We further analyzed the filament compressive Young's modulus in the logarithmic spirals using AFM mechanical mapping and found that inner thin and outer thick filament turns had a comparable elasticity of ~7 MPa, with a slight stiffening of the filament towards the spiral center (Extended Data Fig. 4). Both filament thickening as a function of contour length and patch formation indicated that lateral inter-strand interactions were occurring, which in extreme cases can lead to VIPP1 polygonal carpets. To confirm that thick filaments and carpets were indeed the result of lateral filament stacking, we performed a force-sweep experiment.

We found that thick filaments could be split into unitary filaments by increased force and that unitary filaments could anneal at low force (Fig. 2h–k and Supplementary Video 8).

VIPP1 forms regular polygons

In stark contrast to canonical ESCRT-III spirals, VIPP1 also formed regular polygons on lipid bilayers (Fig. 3a,b and Supplementary Video 9). When unperturbed, VIPP1 tended to form regular polygons in which all vertices were connected by straight intersector boundaries that converged towards the center. Quantification of the symmetry of VIPP1 polygons yielded a distribution dominated by octagons and decreasing populations of polygons with higher-order symmetry, up to dodecagons. Notably, polygons with fewer than eight sides were never detected (Fig. 3c). Thus, the radially aligned subunits in individual carpets in neighboring polygon sectors had an angle difference of 45° in octagons, with molecular constraints apparently allowing angle changes of only 45° or less. From the polygon count, we conclude that the octagon represents a lower-energy state than do the higher-symmetry polygons.

In 13% of all imaged VIPP1 assemblies, the central region of the polygons was composed of a VIPP1 filament spiral (Fig. 3a), and 20% of all imaged VIPP1 assemblies yielded polygons without a spiral center (Fig. 3b and Supplementary Video 9). We also observed spirals in which some filament segments far away from the spiral center formed structures reminiscent of polygonal carpets (Fig. 2f), so we hypothesized that, at a certain radius of curvature, the lateral annealing of subunits into carpets becomes as likely as the formation of wide filaments with low curvature. We thus measured the equivalent radius (Fig. 3a), where the transition between morphologies in mixed spiral–polygon architectures occurs, and found a positive correlation between the equivalent radius and number of polygon sides (Fig. 3d).

The intersector boundaries had a clear topographic signal, so we could measure the inclusion angles and assess how regular the geometries of the VIPP1 polygons were. We identified the boundaries computationally using the Hough transform and plotted the inclusion-angle distributions in the different polygon types (Fig. 3e and Extended Data Fig. 5). All distributions were well-fitted by one Gaussian, except the distribution of dodecagons, which encompassed too few events. Fitting the inclusion-angle data by a power law model yielded the exponent k = -1.0, which corroborated the inverse relationship between inclusion angle and the number of polygon sides (Fig. 3f). Thus, all results support the notion that VIPP1 polygons tend to have a regular shape. This means that the entire VIPP1 polygon must be one physical object in which the geometrical information is encoded over its entire size, often >1 μm (Fig. 3a,b). Thus, we hypothesize that the geometrical information is set by the equivalent radius in the case of the mixed spiral-polygon architectures, or in the central polymerization hub for completely regular polygons. In this case, the innermost ring should have an oligomeric state that is related to the overall geometry of the polygon, for example, a ring comprising 8, 16, 24 or 32 subunits for the most prevalent octagons. Alternatively, spiral-polygons could slowly transform into polygons through inward lateral annealing of strands.

We also imaged the surface of the polygons at high resolution (Fig. 3g and Supplementary Video 10) and found periodic striations, with a periodicity of -4.8 nm (Fig. 3h), in agreement with the periodicity in VIPP1 spirals (Fig. 2g). Although the subunit periodicity within each sector was uniform, we found abrupt orientational changes at the intersector boundaries, in contrast to the continuous longitudinal bending in spirals. The average protrusion height of the intersector boundaries above surrounding sectors was only -0.4 nm (Extended Data Fig. 6). Thus, the boundaries likely represent a tilted subunit orientation in which the filaments are kinked to accommodate the different orientations of 2D carpets in each polygon sector. We hypothesize that these tilted orientations come with an energy cost.

To get further insights into the structure and physical properties of the 2D carpets in the VIPP1 polygon sectors, we applied again

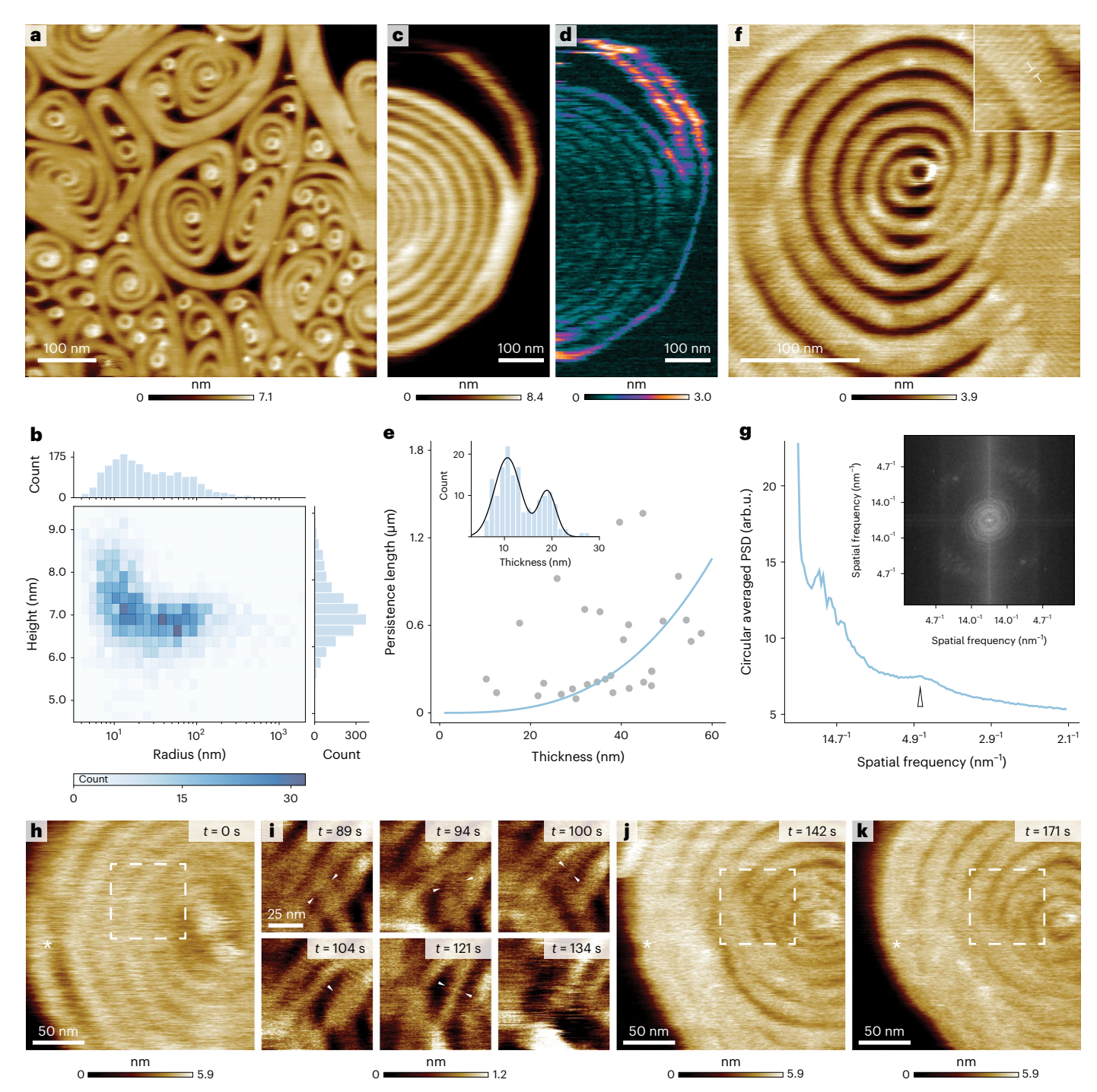


Fig. 2 | **VIPP1** spirals consist of flexible filaments with constant periodicity but variable thickness. a, Overview HS-AFM image of matured VIPP1 spirals on membranes. **b**, Filament height versus radius of curvature distribution. False color scale, event count. **c**, Projection average of six consecutive HS-AFM frames showing a VIPP1 spiral. **d**, Projection map of the s.d. of the frames averaged in **c**, illustrating the flexibility of the free distal filament end. **e**, Persistence lengths of free filament ends versus filament thickness fitted using the elastic rod model. Inset, spiral filament thickness distribution. **f**, High-resolution HS-AFM image of a representative VIPP1 spiral, with central ring, increasing filament thickness as a function of spiral filament contour length and characteristic subunit periodicity (inset). **g**, Power spectrum density (PSD) of the image in **f**. The arrowhead indicates the local maximum corresponding to VIPP1 filament periodicity of

4.8 nm. Inset, two-dimensional (2D) power spectrum of ${\bf f}$. arb.u., arbitrary units. ${\bf h}$ - ${\bf k}$, Force-sweep HS-AFM experiment showing that thick filaments are stacks of laterally annealed filaments. In HS-AFM force-sweep experiments, a specific region in the scanning field is scanned at increased force. Upon zooming out and performing imaging with minimal force, the effects of the force application on the molecular structure can be observed. Thick VIPP1 filaments (${\bf h}$) disassociate under force (${\bf i}$) into thinner filaments (${\bf j}$) and reassociate (${\bf k}$) into thicker filaments after the force is minimized. Filaments in the vicinity fused into a continuous carpet during this invasive experiment, corroborating the finding that filaments can laterally anneal (laterally annealing filaments are marked with asterisks in ${\bf h}$, ${\bf j}$ and ${\bf k}$).

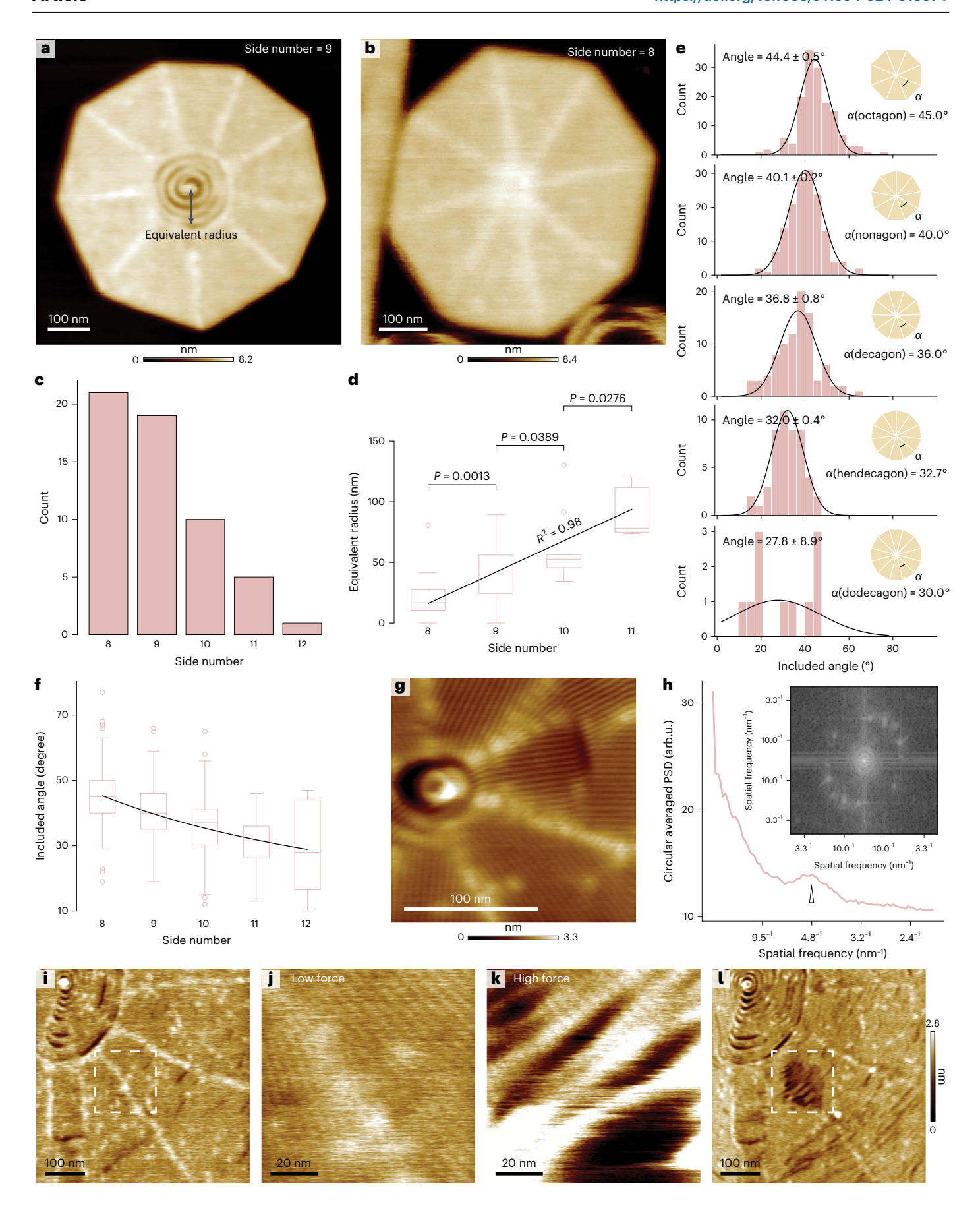


Fig. 3 | **Regular VIPP1 polygons consist of sectors with subunits organized in 2D arrays that are stacks of filaments. a,b**, HS-AFM images of mixed spiral-polygon (**a**) and polygon (**b**) VIPP1. Intersector boundaries are clearly visible. **c**, Histogram of polygons with different numbers of sides (symmetries). **d**, Boxplots of equivalent radii of polygons with different numbers of sides (octagon, n = 21; nonagon, n = 19; decagon, n = 10; hendecagon, n = 5). The equivalent radius is the radius at which the spiral transitions into a polygon (see **a**). Box, Q1 to Q3; line, median. Top whisker, Q3 + 1.5 × IQR; bottom whisker, Q1 – 1.5 × IQR; circles, outliers. P values were determined by one-sided t-test. **e**, Histograms of inclusion angles at the vertices of corresponding polygons (black curves, Gaussian fits). Inclusion angles of regular polygons are shown in the upper right corner. **f**, Boxplots of inclusion angles of polygons with

different numbers of sides (octagon, n = 147; nonagon, n = 152; decagon, n = 90; hendecagon, n = 50; dodecagon, n = 11). The mean values from each group were fitted by a power law function, $y = 360 \times x^k$, yielding k = -1.0. Box, Q1 to Q3; line, median. Top whisker, Q3 + 1.5 × IQR; bottom whisker, Q1 - 1.5 × IQR; circles, outliers. \mathbf{g} , High-resolution image of a VIPP1 polygon. \mathbf{h} , PSD of image in \mathbf{g} . The arrowhead indicates a VIPP1 subunit periodicity of 4.8 nm. Inset, 2D power spectrum of \mathbf{g} . \mathbf{i} - \mathbf{l} , Force-sweep HS-AFM experiment showing that the 2D arrays are constituted of laterally stacked filaments. Imaging of polygon at minimal force (\mathbf{i}), application of increased force to an imaging sub-area covering the interface of two polygon sectors at low (\mathbf{j}) and high (\mathbf{k}) force, and observation of force-induced changes in VIPP1 organization (\mathbf{l}).

a force-sweep HS-AFM experiment. We found that, under force, the 2D carpets of sectors and the boundary disintegrated, but filaments remained intact (Fig. 3i–l and Supplementary Video 11). Thus, the inter-molecular longitudinal interactions along the filament are stronger than the lateral interactions. The 2D carpets in the polygon sectors are thus stacks of filaments.

We developed an analytical model that evaluates the competition of spiral and polygonal filament shapes considering filament bending, intersector boundary, and lateral annealing energy components (Supplementary Note 1). This model explains how, at low curvatures, the lateral annealing and the resulting formation of 2D arrays in polygons can become dominant despite the energy cost associated with the intersector boundaries. Furthermore, the model provides quantitative predictions for the equivalent radius and how the equivalent radius increases with increased polygon symmetry.

VIPP1 spiral and polygon growth processes and kinetics

HS-AFM images revealed that VIPP1 adopts two distinct supramolecular structures, but what about their growth dynamics? To get insights into the assembly-specific polymerization processes of VIPP1, we measured the area and perimeter of isolated VIPP1 polymers in continuous HS-AFM frames.

First, we investigated the growth dynamics of spirals. The growth of VIPP1 spirals was divided into nucleation and growth periods (Fig. 4a). Additionally, the growth period could be further divided into a fast-growing and slow-growing period, with area growth rates of $0.074 \,\mu\text{m}^2 \,\text{min}^{-1}$ and $0.012 \,\mu\text{m}^2 \,\text{min}^{-1}$, respectively (Fig. 4b). A typical growth curve of a VIPP1 spiral together with corresponding spiral images at different time points revealed that the spiral was rather loosely packed during the fast-growing period, and then densified during the slow-growing period (Fig. 4c). To quantify the compactness of spirals, we considered a dimensionless measure of the inverse spiral density, perimeter² / $(4\pi \times area)$, in which the perimeter and area were measured from the spiral segmentation. When the spiral was loose (for example, stage 2 in Figure 4c), empty spaces were present within the spiral segmentation, and the inverse density ratio was larger than 1, whereas the combined distributions of area growth rate and inverse density ratio had a positive correlation (Extended Data Fig. 7). This supported the notion that the spiral growth rate was dependent on self-crowdedness, resulting in a two-stage growth process.

Adding to the complexity of the polymerization process, the height of VIPP1 spirals also changed slightly as the polymerization process proceeded (Fig. 4d). In the nucleation stage, the height of VIPP1 spirals decreased from >10 nm to -4 nm, likely representing the collapse of a nucleation ensemble at the center of VIPP1 assemblies, that might be reminiscent of the rings and baskets observed in cryo-EM, into filaments that were just one subunit high (Fig. 4d, gray). This event was followed by a growth period as the spiral size increased, during which the height increased from -4 nm to -8 nm (Fig. 4d, blue). The height increase with spiral growth and densification likely documents a conformational rearrangement of VIPP1 as it undergoes polymerization and spiral densification.

Subsequently, we investigated the growth dynamics of polygons. Polygons grew much faster than spirals, some at >0.5 μm^2 min $^{-1}$ (Fig. 4e). Because polygons are also mono-molecular layers, the perimeter of polygons should, provided that polygons grow primarily at their perimeter, correspond to the one-dimensional solvent-accessible surface area (SASA), and so should correlate with the area growth rate. To evaluate this correlation, we separated perimeters by length and calculated the mean values of area growth rates of each group. The data could be fitted linearly with a slope of 1.1 \pm 0.1 nm s $^{-1}$ (fit value \pm fitting error, Fig. 4f), supporting the notion that multiple VIPP1 filaments grew along the periphery of polygons (see Methods). Using dynamic HS-AFM imaging, we observed such peripheral growth (Fig. 4g and Supplementary Video 12). Thus, dynamic imaging and growth kinetics analysis agree with polygonal growth at the periphery through simultaneous filament polymerization in each polygon sector.

Finally, we acquired HS-AFM videos of mixed spiral–polygon assembly growth: these structures first follow spiral growth, showing a two-stage growth process with a fast-growing loose spiral stage and a slow-growing densification stage, and then, as a critical radius is reached, show a transition to a polygon shape with fast peripheral growth (Fig. 4h and Supplementary Video 13).

VIPP1 filament mechanics drive the assembly

After revealing that VIPP1 polymerized along the periphery in polygons, we investigated the spiral growth process in detail. First, we

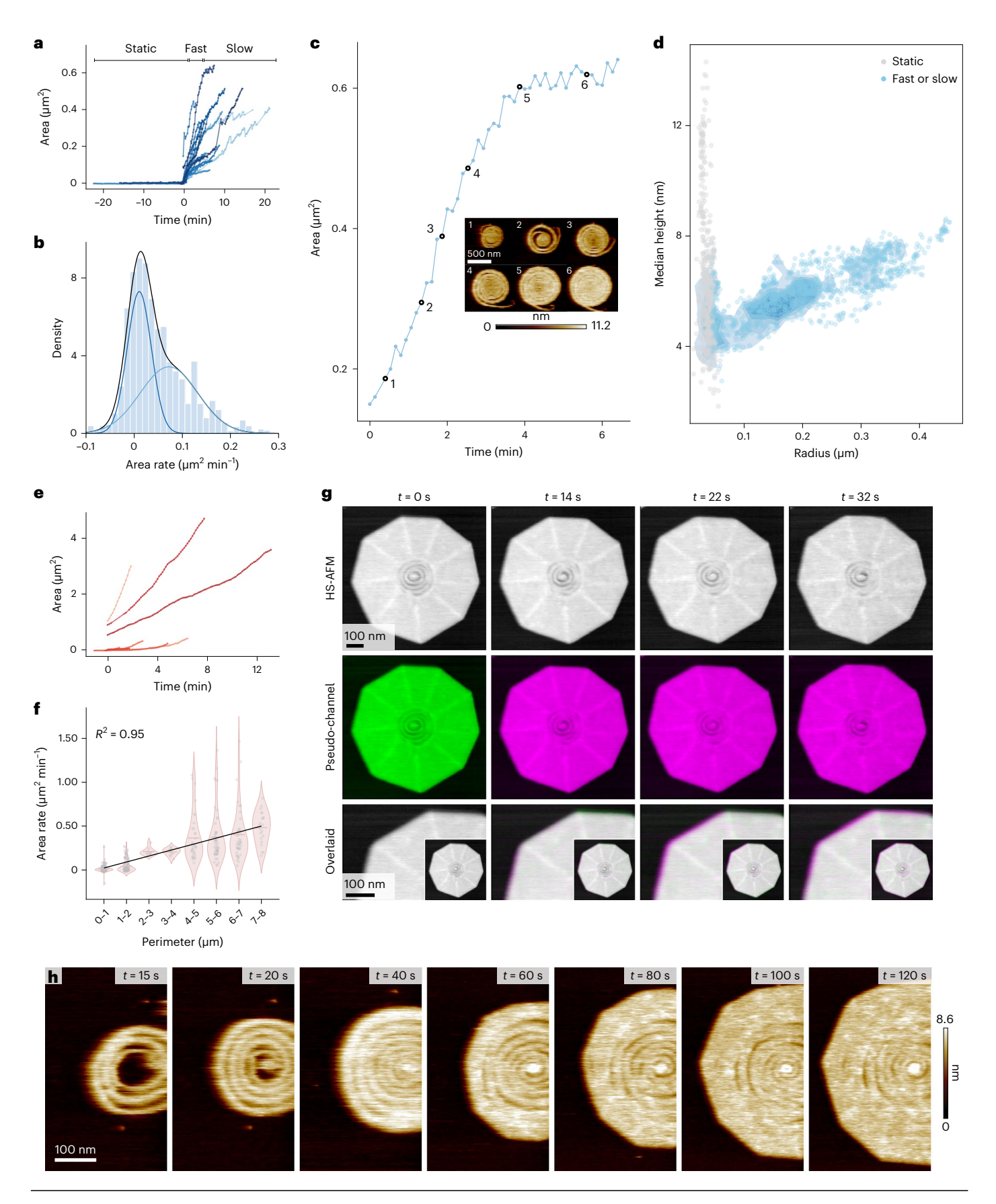
Fig. 4 | VIPP1 growth kinetics are dependent on assembly geometry.

 $\label{eq:approx} \textbf{a}, Growth curves representing the changes in area of isolated VIPP1 spirals over time. The growth process was divided into a nucleation period, a fast-growing stage and a slow-growing stage. <math display="block"> \textbf{b}, \text{ Histogram of area growth rates in } \textbf{a}. \text{ The distribution was fitted by two Gaussians, which yielded a fast-growing rate of } 0.074 \pm 0.012 \, \mu\text{m}^2\,\text{min}^{-1} \text{ and a slow-growing rate of } 0.012 \pm 0.001 \, \mu\text{m}^2\,\text{min}^{-1}, \text{ respectively (fit value} \pm \text{fitting error).} \textbf{c}, \text{ Typical area growth curve of a spiral with fast- and slow-growing stages. Inset, corresponding HS-AFM images at various time points.} \textbf{d}, \text{ 2D histogram of spiral height and radius (gray, nucleation stage; blue, fast- or slow-growing stages).} \textbf{e}, \text{ Area growth curves of isolated VIPP1 polygons.} \textbf{f}, \text{ Violin plots of VIPP1 polygon area growth rates in different groups of VIPP1 polygons with different perimeters.} \text{ Bars indicate the mean area}$

growth rate of each group. Mean area growth rates were fitted by a linear model, which yielded the radius growth rate $1.1\pm0.1\,\mathrm{nm\,s^{-1}}$ (fit value \pm fitting error, see Methods). **g**, HS-AFM images of VIPP1 polygon growth. The image at time t=0 s was projected into a green channel, and subsequent images were projected into a magenta channel. The image overlay illustrates the growing filament along the periphery in the magenta channel (consistent pixels add up to be gray). Top, HS-AFM images at different time points. Middle, image at time t=0 s (green), and all subsequent images (magenta). Bottom, enlarged view of the growing filament (inset, overlaid images). **h**, Mixed spiral–polygon growth. A loosely packed spiral densified, and upon reaching a critical equivalent radius, transitioned into peripheral polygonal growth.

considered the behavior of some spirals in which the peripheral end remained at a fixed position after nucleation (likely owing to a small defect in the SLB) (Fig. 5a). In this case, the growth pattern exhibited a directional boundary profile (Fig. 5b). By setting the fastest-growing

direction of the boundary profiles of this class of spirals to the angle 180°, we obtained the distribution of distances from nucleation site to boundaries as time proceeded (Fig. 5c): the distance distribution gradually widened in a time-dependent manner, ultimately reaching



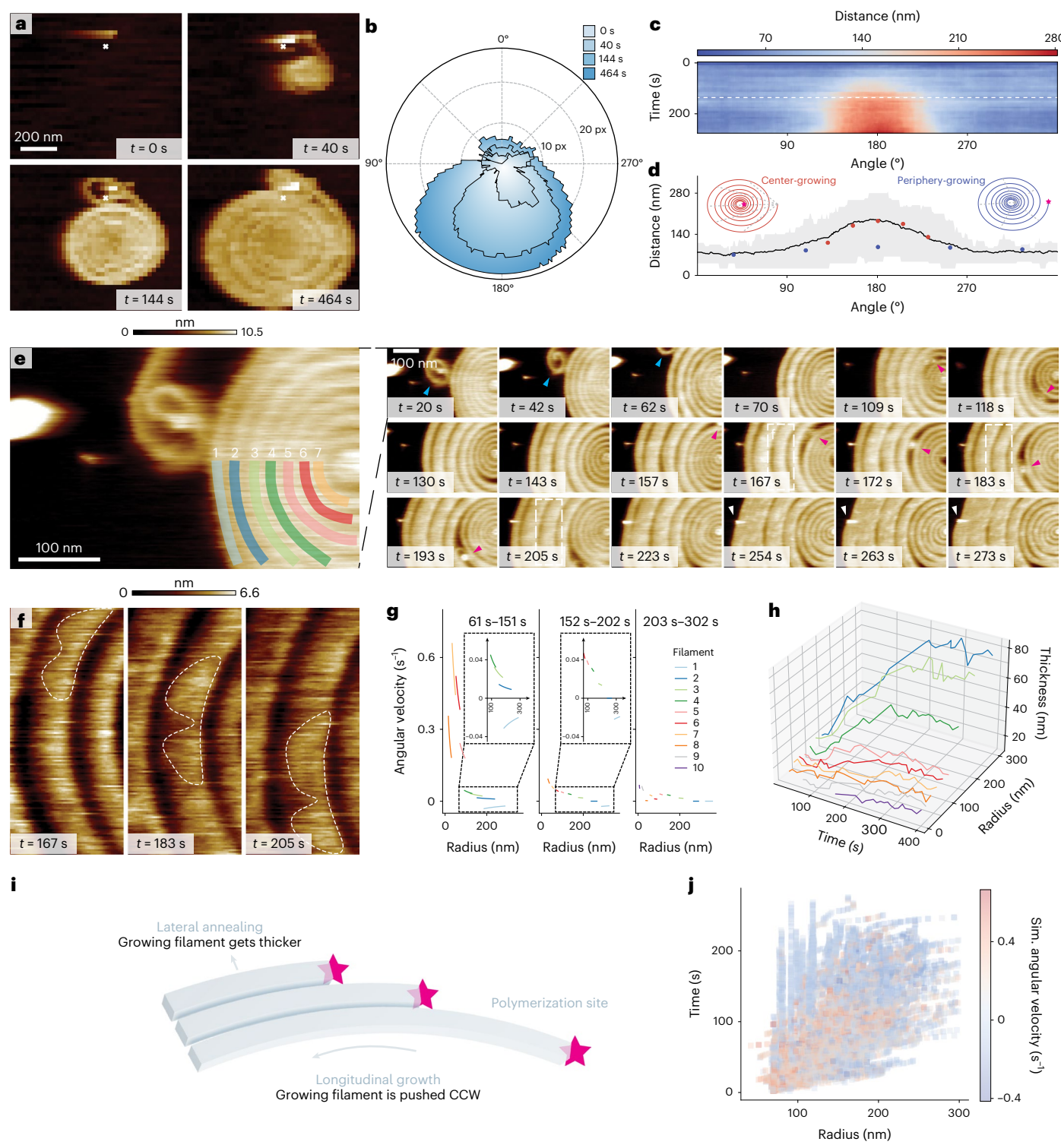


Fig. 5 | VIPP1 spiral growth mechanism. a, HS-AFM images of a spiral growing with a static distal filament end (white cross). **b**, The boundary profile of the spiral in **a**. The fixed distal end was used as the origin of the polar coordinate system. **c**, Distance distribution from origin to spiral boundary. False color scale, average distance. **d**, Cross-section along white dashed line in **c**. Black line, average distance (n = 16). Gray region, distance interquartile range. Insets, models of center-growing (red, polymerization occurs in the spiral center) and peripherygrowing (blue, polymerization occurs at the peripheral filament tip) spirals. The growing ends of the filaments are indicated by stars. Distance from spiral ends to spiral boundaries (gray dashed lines in models) are shown as red and blue dots. **e**, HS-AFM images of a spiral growing with resolved filament rotation (Supplementary Video 14). Left, close-up view with labeled filaments. Right, HS-AFM video frames of the growing spiral. The distal end of the spiral rotated

CW (cyan arrowheads), and inner filaments rotated CCW (magenta arrowheads). Eventually, the spiral encountered an obstacle (white arrowheads), and growth stopped. **f**, Enlarged and contrast-enhanced region (white box in **e**) with CCW filament flow. **g**, Angular velocity of filament turns decayed over radius and time. The analysis is grouped in three periods during spiral growth, with CCW rotation defined as positive. The angular velocity of the outermost turn and distal end had opposite CW directions. **h**, Filament thickness and radius as a function of time (colors as in **e**). **i**, Schematic, two types of VIPP1 subunit binding reactions occur during spiral maturation. Longitudinal binding to the tip leads to lengthening, and lateral outwards annealing leads to thickening of the filament. **j**, In a Monte Carlo simulation, angular velocity decayed with radius of curvature and time (Supplementary Video 16).

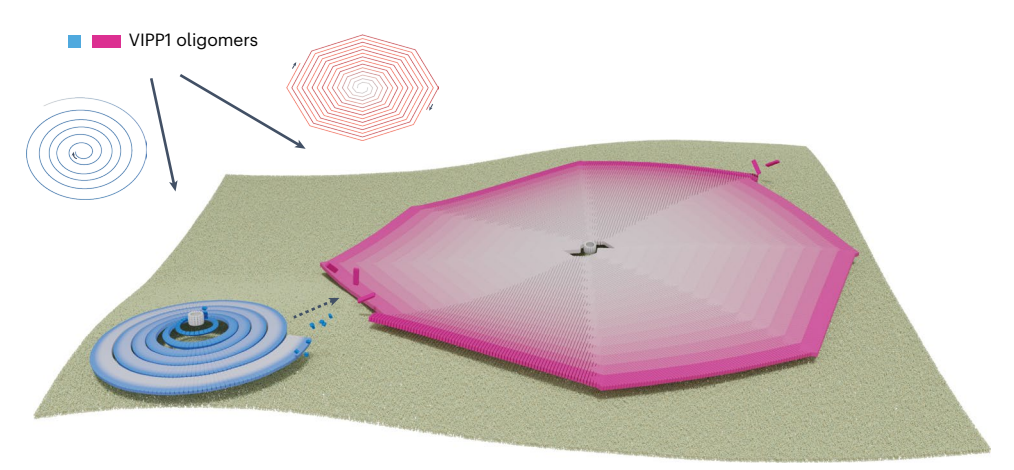


Fig. 6 | **Schematic of the VIPP1 assembly in spirals and polygons.** Freely diffusing VIPP1 subunits assemble in filaments to form spirals, where subunits polymerize to a ring-shaped polymerization hub at the spiral center, and polygons, where subunits polymerize peripherally in discrete sectors. Filaments grow CW in both spirals and polygons. In spirals, filaments are pushed outwards

leading to a CCW subunit flow. In polygons, filaments are added CW at the periphery. Spirals are initially Archimedean and change their geometry to logarithmic through radius-dependent and time-dependent lateral annealing of subunits to outermore turns. Older subunits are colored in gray, and newly added subunits are colored in blue or pink in spirals or polygons, respectively.

approximately 90° at its maximum width. Concurrently, the distance itself also increased over time, reflecting the expanding boundary of spirals. For interpretation, we simulated two spiral growth models, where the filament grows either at the center or at the periphery. Only the center-growing model was in good agreement with the experiment (Fig. 5d). Second, we analyzed the behavior of spirals that did not move overall, but displayed rotational freedom, illustrated by movements of the peripheral end and topographic flow along the spiral filament (Fig. 5e). Initially, the right-handed spiral had 7 turns, consisting of a thin filament (Fig. 5e, left, and t = 20 s). As the spiral grew, the peripheral filament rotated CW around the spiral (Fig. 5e, t = 20 s to 70 s, cyan arrowheads), in line with previous observations (Fig. 1e). Taking advantage of heterogeneities in the filament morphology and a topographic inclusion between two turns at approximately half the spiral radius, we analyzed the processive flow of the spiral filament during growth. The filament flow rotated counter-clockwise (CCW) (Fig. 5e, t = 109 s to 193 s, magenta arrowheads). Contrast enhancement revealed unambiguously the CCW filament flow in the right-handed spiral from the center to the periphery (Fig. 5f and Supplementary Video 14).

It is intuitive that, in right-handed spirals that polymerize at their center, the rotation angular velocity, that is the filament CCW flow, of spiral turns slows with increasing distance from the center. To quantify filament rotation, we analyzed each filament over time and extracted its angular velocity, thickness and radius of curvature (Extended Data Figs. 8 and 9). In general, the angular velocities in the first period were larger than those in the later periods (Fig. 5g), consistent with the observed slowing of the growth and densification of spirals. Indeed, the thickness of the filaments increased over time and as the radius increased (Fig. 5h). As expected, the angular velocity of the filament turns scaled inversely with their radius from the center. Notably, the outermost turn and the free distal end showed opposite, CW rotation (Fig. 5g, insets). As subunits are added at the spiral center, the innermost turns with a small radius and short length have a fast CCW angular filament flow, whereas turns at a larger radius have slower angular displacements. Knowing the angular velocity of the filament flow at any given radius from the spiral center, we calculated the filament extension speed, ~27 nm s⁻¹, and with the knowledge of the subunit periodicity in the filaments, ~4.8 nm, we estimate a polymerization rate of ~5.6 VIPP1 subunits per second at a 2 μM concentration. But how can it be that the outermost turn rotates CW? To understand this phenomenon, we modeled Archimedean, logarithmic and dynamic logarithmic spirals (Supplementary Note 2 and Supplementary Video 15).

Only in the dynamic logarithmic spiral model did the peripheral turn and distal end begin to turn CW with maturation, because the continuous outward lateral annealing of subunits increases the thickness of filament turns in a time-dependent manner.

We thus propose the following polymerization model: new VIPP1 subunits bind at the polymerization hub in the spiral center. Initially, spiral growth is Archimedean. However, as polymerization progresses and lower-curvature turns emerge, subunits anneal laterally to filaments, making them thicker, linearly with the filament contour length. This leads to the transformation into logarithmic spirals (Fig. 5i, see 'Discussion'). We simulated (n = 100) the growth process using the lattice Monte Carlo method⁴⁷. The distribution of simulated angular velocities demonstrated a decay and even a change of direction over time and with respect to radius length (Fig. 5j, Supplementary Note 3 and Supplementary Video 16), in agreement with our experiments.

Discussion

Recent cryo-EM studies have reported structures of VIPP1 assembled in helical rods and ring-stacked baskets^{14,17}. Here, we show two typical supramolecular structures that are formed spontaneously by VIPP1 on membranes that are highly enriched with negatively charged lipids: spirals and polygons. In addition, mixed architectures occurred that were characterized by a spiral center and polygonal periphery. On the basis of our findings, we propose the following VIPP1 polymerization model: freely bulk-diffusing VIPP1 that is monomeric, of low oligomeric state or occasionally forms rings²² polymerizes CW at a ring-shaped hub into filaments and forms right-handed spirals. The center-growing spiral polymerization is in stark contrast to eukaryotic ESCRT-III polymerization³⁴. VIPP1 spirals are initially Archimedean, in agreement with the eukaryotic ESCRT-III spiral architecture. However, as the spirals mature, they densify through lateral annealing of subunits, with the filament thickness scaling linearly with the filament contour length (Fig. 6). It has been reported that the most tapered top two layers of VIPP1 baskets can bind and hydrolyze trinucleotides¹⁴, which could play a part in reshaping the filament curvature in spirals. From filament fluctuation analysis, we estimate the elastic modulus of VIPP1 filaments to be ~34 kPa, whereas matured filament strands harden through lateral annealing, which might be functionally reminiscent of the multi-component filaments in the eukaryotic ESCRT-III system⁴⁵. Notably, VIPP1 polymers are disassembled in chloroplasts by the chaperones HSP70B-CDJ2-CGE1 in the presence of ATP⁴⁸, which might be reminiscent of the action of Vps4 in ESCRT-III filament turnover³⁸.

We also observed that VIPP1 spiral height decreased during the initial nucleation stage and then gradually increased during growth. In VIPP1 ring structures, the protein was observed in an open conformation^{14,17}, in agreement with structures of ESCRT-III^{26,28,45}. In addition, it was shown that a short polypeptide derived from the amino-terminal membrane-binding region of VIPP1 was unstructured but acquired an α -helical fold upon interaction with lipid⁴⁹. We hypothesize that the early height decrease, and later height increase during spiral growth, could be related to conformational rearrangements in VIPP1 upon lipid binding and polymerization. In most ESCRT-III filaments 28,29,32,37,40,50 and in VIPP1 rings 14,17, subunits make lateral inter-helical contacts to form elongated polymers. Here, using HS-AFM, we observe a conserved subunit periodicity of ~4.8 nm. in excellent agreement with the periodicity in the top rings in the baskets (ranging from 51 Å in the C14 basket to 48 Å in the C18 basket). We thus hypothesize that the longitudinal arrangement of VIPP1 subunits is preserved within all supramolecular architectures and is similar to that of all ESCRT-III polymers.

VIPP1 forms micrometer-size regular polygons in which each polygon sector is composed of a 2D array of subunits through lateral association of strands. Similar VIPP1 carpet structures have been observed and reported to protect membranes in another in vitro study²⁰. For comparison, other ESCRT-III polymers have shown only limited lateral association. The deletion of the C terminus of Snf7 enhances the lateral association and leads to tightened spirals 32,35. Similarly, CHMP2A lacking the C terminus has been observed to acquire the ability to form polymers⁵¹. In VIPP1, deletion of the C terminus causes excessive lateral association⁸. Although it has been challenging to determine the homology of the C-terminal regions between VIPP1 and Snf7 (ref. 17), these results suggest a conserved regulatory function of the C-terminal regions in the formation of VIPP1 and eukaryotic ESCRT-III supramolecular structures. Nonetheless, VIPP1 polygons display a novel ESCRT-III superfamily polymer architecture. The observed polygon size could be too large and their architecture too static to be physiologically relevant. Nevertheless, they underscore the unique propensity of VIPP1 to engage lateral annealing of filament strands. In addition, the evaluation of the mixed spiral-polygon structures and their transition at a critical radius allowed us to estimate a radius of ~80 nm as a potential upper bound for the size of spirals. Further research is needed to understand the function of the polygons. However, eukaryotic ESCRT-III has been shown to be associated with a wide variety of functions that might seem conflicting, such as membrane fission and repair³¹, and thus VIPP1 spirals and polygons could represent architectures related to different functions. Another interesting region in the VIPP1 protein is the N-terminal amphipathic helix. It should be anticipated that mutations in this region will impact VIPP1 membrane association and the nucleation and architecture of VIPP1 assemblies¹⁴. Again, further research is needed to address the precise role of this region in VIPP1 assembly and function. HS-AFM could be particularly useful for future studies of mutants, because it provides dynamic information and thus allows researchers to investigate which steps of the nucleation, growth, assembly and maturation processes are impacted by mutations.

In summary, our study provides evidence that VIPP1 is more similar to canonical ESCRT-III proteins than the initial reports of the stacked ring baskets and helical rods might have suggested. Indeed, VIPP1 forms elastic filaments that assemble into ESCRT-III-like spirals. However, several aspects of supramolecular VIPP1 assemblies, such as the polymerization process, the preserved handedness of spirals, the radius- and time-dependent filament thickening and the formation of polygonal arrays, are different from what has been observed for eukaryotic ESCRT-III. Further studies are needed to elucidate how the various supramolecular architectures connect to membrane remodeling and downstream activity triggered by VIPP1.

Online content

Any methods, additional references, Nature Portfolio reporting summaries, source data, extended data, supplementary information, acknowledgements, peer review information; details of author contributions and competing interests; and statements of data and code availability are available at https://doi.org/10.1038/s41594-024-01367-7.

References

- Mullineaux, C. W. Co-existence of photosynthetic and respiratory activities in cyanobacterial thylakoid membranes. *Biochim*. *Biophys. Acta* 1837, 503–511 (2014).
- Li, H.-m, Kaneko, Y. & Keegstra, K. Molecular cloning of a chloroplastic proteinassociated with both the envelope and thylakoid membranes. *Plant Mol. Biol.* 25, 619–632 (1994).
- Kroll, D. et al. VIPP1, a nuclear gene of Arabidopsis thaliana essential for thylakoid membrane formation. Proc. Natl Acad. Sci. USA 98, 4238–4242 (2001).
- Westphal, S., Heins, L., Soll, J. & Vothknecht, U. C. Vipp1 deletion mutant of Synechocystis: a connection between bacterial phage shock and thylakoid biogenesis? Proc. Natl Acad. Sci. USA 98, 4243–4248 (2001).
- Fuhrmann, E. et al. The vesicle-inducing Protein 1 from Synechocystis sp PCC 6803 organizes into diverse higher-ordered ring structures. Mol. Biol. Cell 20, 4620–4628 (2009).
- Gutu, A., Chang, F. & O'Shea, E. K. Dynamical localization of a thylakoid membrane binding protein is required for acquisition of photosynthetic competency. *Mol. Microbiol.* 108, 16–31 (2018).
- 7. Nordhues, A. et al. Evidence for a role of VIPP1 in the structural organization of the photosynthetic apparatus in *Chlamydomonas*. *Plant Cell* **24**, 637–659 (2012).
- Zhang, L. G., Kondo, H., Kamikubo, H., Kataoka, M. & Sakamoto, W. VIPP1 has a disordered C-terminal tail necessary for protecting photosynthetic membranes against stress. *Plant Physiol.* 171, 1983–1995 (2016).
- 9. Bryan, S. J. et al. Localisation and interactions of the Vipp1 protein in cyanobacteria. *Mol. Microbiol* **94**, 1179–1195 (2014).
- Fuhrmann, E., Gathmann, S., Rupprecht, E., Golecki, J. & Schneider, D. Thylakoid membrane reduction affects the photosystem stoichiometry in the cyanobacterium Synechocystis sp. PCC 6803. Plant Physiol. 149, 735–744 (2009).
- Gao, H. & Xu, X. D. Depletion of Vipp1 in Synechocystis sp PCC 6803 affects photosynthetic activity before the loss of thylakoid membranes. FEMS Microbiol. Lett. 292, 63–70 (2009).
- Aseeva, E. et al. Vipp1 is required for basic thylakoid membrane formation but not for the assembly of thylakoid protein complexes. *Plant Physiol. Biochem.* 45, 119–128 (2007).
- 13. Zhang, L., Kato, Y., Otters, S., Vothknecht, U. C. & Sakamoto, W. Essential role of VIPP1 in chloroplast envelope maintenance in *Arabidopsis*. *Plant Cell* **24**, 3695–3707 (2012).
- Gupta, T. K. et al. Structural basis for VIPP1 oligomerization and maintenance of thylakoid membrane integrity. Cell 184, 3643– 3659 (2021).
- Aseeva, E. et al. Complex formation of Vipp1 depends on its alpha-helical PspA-like domain. J. Biol. Chem. 279, 35535–35541 (2004).
- Saur, M. et al. A Janus-Faced IM30 ring involved in thylakoid membrane fusion is assembled from IM30 tetramers. Structure 25, 1380–1390 (2017).
- 17. Liu, J. et al. Bacterial Vipp1 and PspA are members of the ancient ESCRT-III membrane-remodeling superfamily. *Cell* **184**, 3660–3673 (2021).
- Theis, J. et al. VIPP1 rods engulf membranes containing phosphatidylinositol phosphates. Sci. Rep. 9, 8725 (2019).
- 19. Hennig, R. et al. IM30 triggers membrane fusion in cyanobacteria and chloroplasts. *Nat. Commun.* **6**, 7018 (2015).

- Junglas, B. et al. IM30 IDPs form a membrane-protective carpet upon super-complex disassembly. Commun. Biol. 3, 595 (2020).
- Junglas, B. et al. Membrane destabilization and pore formation induced by the Synechocystis IM30 protein. Biophys. J. 121, 3411–3421 (2022).
- Heidrich, J. et al. Organization into higher ordered ring structures counteracts membrane binding of IM30, a protein associated with inner membranes in chloroplasts and cyanobacteria. J. Biol. Chem. 291, 14954–14962 (2016).
- Vietri, M., Radulovic, M. & Stenmark, H. The many functions of ESCRTs. Nat. Rev. Mol. Cell Biol. 21, 25–42 (2020).
- Schoneberg, J., Lee, I. H., Iwasa, J. H. & Hurley, J. H. Reverse-topology membrane scission by the ESCRT proteins. *Nat. Rev. Mol. Cell Biol.* 18, 5–17 (2017).
- 25. Junglas, B. et al. PspA adopts an ESCRT-III-like fold and remodels bacterial membranes. *Cell* **184**, 3674–3688 (2021).
- 26. Bajorek, M. et al. Structural basis for ESCRT-III protein autoinhibition. *Nat. Struct. Mol. Biol.* **16**, 754–762 (2009).
- Henne, W. M., Buchkovich, N. J., Zhao, Y. & Emr, S. D. The endosomal sorting complex ESCRT-II mediates the assembly and architecture of ESCRT-III helices. Cell 151, 356–371 (2012).
- Tang, S. et al. Structural basis for activation, assembly and membrane binding of ESCRT-III Snf7 filaments. eLife 4, e12548 (2015).
- McCullough, J. et al. Structure and membrane remodeling activity of ESCRT-III helical polymers. Science 350, 1548–1551 (2015).
- Huber, S. T., Mostafavi, S., Mortensen, S. A. & Sachse, C. Structure and assembly of ESCRT-III helical Vps24 filaments. Sci. Adv. 6, eaba4897 (2020).
- Jukic, N., Perrino, A. P., Redondo-Morata, L. & Scheuring, S. Structure and dynamics of ESCRT-III membrane remodeling proteins by high-speed atomic force microscopy. *J. Biol. Chem.* 299, 104575 (2023).
- 32. Shen, Q. T. et al. Structural analysis and modeling reveals new mechanisms governing ESCRT-III spiral filament assembly. *J. Cell Biol.* **206**, 763–777 (2014).
- 33. Chiaruttini, N. et al. Relaxation of loaded ESCRT-III spiral springs drives membrane deformation. *Cell* **163**, 866–879 (2015).
- Jukic, N., Perrino, A. P., Humbert, F., Roux, A. & Scheuring, S. Snf7 spirals sense and alter membrane curvature. *Nat. Commun.* 13, 2174 (2022).
- 35. Hanson, P. I., Roth, R., Lin, Y. & Heuser, J. E. Plasma membrane deformation by circular arrays of ESCRT-III protein filaments. *J. Cell Biol.* **180**, 389–402 (2008).
- Banjade, S., Tang, S., Shah, Y. H. & Emr, S. D. Electrostatic lateral interactions drive ESCRT-III heteropolymer assembly. eLife 8, e46207 (2019).
- Azad, K. et al. Structural basis of CHMP2A-CHMP3 ESCRT-III polymer assembly and membrane cleavage. *Nat. Struct. Mol. Biol.* 30, 81–90 (2023).

- 38. Mierzwa, B. E. et al. Dynamic subunit turnover in ESCRT-III assemblies is regulated by Vps4 to mediate membrane remodelling during cytokinesis. *Nat. Cell Biol.* **19**, 787–798 (2017).
- Pfitzner, A. K. et al. An ESCRT-III polymerization sequence drives membrane deformation and fission. Cell 182, 1140–1155 (2020).
- Nguyen, H. C. et al. Membrane constriction and thinning by sequential ESCRT-III polymerization. *Nat. Struct. Mol. Biol.* 27, 392–399 (2020).
- 41. Eme, L. et al. Inference and reconstruction of the heimdallarchaeial ancestry of eukaryotes. *Nature* **618**, 992–999 (2023).
- 42. Cashikar, A. G. et al. Structure of cellular ESCRT-III spirals and their relationship to HIV budding. *eLife* **3**, eO2184 (2014).
- 43. Priest, L., Peters, J. S. & Kukura, P. Scattering-based light microscopy: from metal nanoparticles to single proteins. *Chem. Rev.* **121**, 11937–11970 (2021).
- Dahmardeh, M., Mirzaalian Dastjerdi, H., Mazal, H., Kostler, H. & Sandoghdar, V. Self-supervised machine learning pushes the sensitivity limit in label-free detection of single proteins below 10 kDa. Nat. Methods 20, 442–447 (2023).
- Pfitzner, A. K., Moser von Filseck, J. & Roux, A. Principles of membrane remodeling by dynamic ESCRT-III polymers. *Trends* Cell Biol. 31, 856–868 (2021).
- Chiaruttini, N. & Roux, A. Dynamic and elastic shape transitions in curved ESCRT-III filaments. Curr. Opin. Cell Biol. 47, 126–135 (2017).
- 47. Gillespie, D. T. A general method for numerically simulating the stochastic time evolution of coupled chemical reactions. *J. Comput. Phys.* **22**, 403–434 (1976).
- 48. Liu, C. et al. The chloroplast HSP70B–CDJ2–CGE1 chaperones catalyse assembly and disassembly of VIPP1 oligomers in *Chlamydomonas*. *Plant J.* **50**, 265–277 (2007).
- McDonald, C., Jovanovic, G., Wallace, B. A., Ces, O. & Buck, M. Structure and function of PspA and Vipp1 N-terminal peptides: insights into the membrane stress sensing and mitigation. *Biochim. Biophys. Acta Biomembr.* 1859, 28–39 (2017).
- 50. Effantin, G. et al. ESCRT-III CHMP2A and CHMP3 form variable helical polymers in vitro and act synergistically during HIV-1 budding. *Cell Microbiol.* **15**, 213–226 (2013).
- Lata, S. et al. Helical structures of ESCRT-III are disassembled by VPS4. Science 321, 1354–1357 (2008).

Publisher's note Springer Nature remains neutral with regard to jurisdictional claims in published maps and institutional affiliations.

Springer Nature or its licensor (e.g. a society or other partner) holds exclusive rights to this article under a publishing agreement with the author(s) or other rightsholder(s); author self-archiving of the accepted manuscript version of this article is solely governed by the terms of such publishing agreement and applicable law.

© The Author(s), under exclusive licence to Springer Nature America, Inc. 2024

Methods

VIPP1 expression and purification

Synechocystis VIPP1 was produced as C-terminal fusion to a chitinbinding domain-intein from plasmid pMS451 in Escherichia coli ER2566 and purified by chitin-affinity chromatography, as described previously14. In brief, a 10 ml overnight culture was diluted into 1 l TB containing 100 mg ml⁻¹ ampicillin and grown at 37°C for 7–8 h. IPTG was then added to a final concentration of 0.5 mM, and growth continued at 18 °C overnight. Cells were collected through a 10-min centrifugation at 5,000g and 4 °C, and were resuspended in 25 ml ice-cold lysis buffer (20 mM HEPES-KOH pH 8.0, 0.5 M NaCl, 1 mM EDTA, 0.1% Triton X-100, Roche cOmplete EDTA-free Protease Inhibitor Cocktail). After sonication on ice, the lysate was centrifuged at 20,000g and 4 °C for 30 min, and the supernatant was passed twice at a flow rate of 0.5 ml min⁻¹through a column with 6 ml chitin beads (NEB) equilibrated with lysis buffer. The column was first washed with 100 ml lysis buffer at 2 ml min⁻¹. A second wash was done using 10 ml KMH buffer (20 mM HEPES-KOH pH 7.6, 80 mM KCl, 2.5 mM MgCl₂) containing 5 mM ATP to remove DnaK binding to VIPP1. After a final wash with 20 ml lysis buffer lacking Triton at 2 ml min⁻¹, the column was flushed with 10 ml cleavage buffer (20 mM Tris-HCl pH 9.0, 0.5 M NaCl, 1 mM EDTA, 50 mM DTT). The column was then gently agitated overnight at room temperature and VIPP1 slowly eluted, and was then flushed with 10 ml KMH buffer for the final elution. The pooled eluate was then concentrated to 5 ml by centrifugation at 4,500g using a Millipore concentrator (AMICON; molecular weight cut-off, 3,000). The concentrate was diluted with 20 ml dialysis buffer and reconcentrated back to 1-2 ml four times: twice with dialysis buffer 1 (20 mM Tris-HCl, pH 7.5, 200 mM NaCl, 75 mM NaSCN) and twice more with dialysis buffer 2 (20 mM Tris-HCl, pH 7.5, 50 mM NaCl, 75 mM NaSCN). Protein concentration was determined using the Bradford assay. The protein was quick-frozen in liquid nitrogen and stored at -80 °C.

SLB preparation

The lipid solution was prepared by mixing DOPC and DOPS in chloroform at a 1:1 ratio (wt/wt), unless otherwise specified, in an amber glass vial. First, the lipid mixture was evaporated under an argon stream while the glass vial was slowly rotated on the vortex mixer to ensure efficient lipid spreading on the inner surface of the glass vial. Then, the vial was placed under a vacuum overnight to remove residual chloroform. Next, imaging buffer (20 mM HEPES-KOH, 80 mM KCl, pH 7.6) was used to rehydrate the lipid at room temperature to a final lipid concentration of 0.3 mg ml⁻¹. The lipid suspension was agitated by vortexing for 1 min, followed by probe sonication (time, 2 min; cycles of 1-s pulses and 1-s rest periods; amplitude, 20%) to form SUVs. The lipid solution was freshly made from rehydration before each HS-AFM experiment. SLBs were deployed on mica as substrate of VIPP1. To form SLBs, 10 µl of adhesion buffer (20 mM HEPES-KOH, 300 mM KCl, pH 7.6) was pipetted on the freshly cleaved mica from one side, and delicate task wiper (Kimtech Science) was used to blot the other side. Then, 10 μl of fresh SUV lipid solution was pipetted on the mica surface in the same way and incubated for 15 min.

HS-AFM imaging

Imaging was performed at room temperature in an amplitude-modulation mode sample-scanning HS-AFM (SS-NEX, RIBM). Short cantilevers (USC-F1.2-k0.15, NanoWorld) with a nominal spring constant of -0.15 N m $^{-1}$ and a resonance frequency of -0.5 MHz in liquid were used, either as-is or with home-made electron beam deposited (EBD) tips. Images were acquired at resolutions ranging from 200 pixels \times 200 pixels to 300 pixels \times 300 pixels. For standard scanning up to 600 nm \times 600 nm, we used a standard HS-AFM scanner (SS-NEX, RIBM), and images were acquired in a range from 0.5 to 1 frame per second (fps). For wide-range scanning up to 7 μ m \times 7 μ m, we used a wide HS-AFM scanner (SS-NEX, RIBM) with an adapted piezo driver capable

of supplying higher voltages and the fps ranged from 0.125 to 0.5. First, 120 μ l of imaging buffer (20 mM HEPES-KOH, 80 mM KCl, pH 7.6) was added into the fluid chamber, and the sample stage, which was covered with SLBs, was put in the fluid chamber using HS-AFM imaging to check the completeness of the SLBs. Next, the sample stage was taken out from the fluid chamber and VIPP1 was added into the fluid chamber to a final concentration of 2 μ M and mixed well by pipetting several times to obtain a homogeneous concentration. The sample stage was then put back into the fluid chamber and data were acquired after a dead time of ~7 min. HS-AFM data were collected in IgorPro using RIBM software packages (Ibis 1.1.0, IgorPro 6.3.7.2). Ten microliters of Milli-Q water were added to compensate for solution evaporation during long experiments. To observe the formation of SLBs on mica in real time, 10 μ l of the SUV lipid solution was added into the fluid chamber of the HS-AFM during scanning.

AFM-based nanomechanical mapping

The compressive Young's modulus of VIPP1 polymers in the z direction was measured using a JPK Nanowizard 4 (Bruker) using cantilevers with a nominal resonance frequency of ~110 KHz and spring constant of 0.25 N m⁻¹ (FASTSCAN-D, Bruker). Lipid SUVs were first incubated on freshly cleaved mica in the sample chamber for ~20 min. Then the chamber was rinsed with imaging buffer more than five times to remove excessive liposomes. VIPP1 was added in the chamber directly to a final concentration of ~0.5 μ M and incubated for ~30 min. The QI mode was used to obtain pixel-by-pixel force-distance curves in the regions of interest (1.5 μ m × 1.5 μ m; 512 pixels × 512 pixels or 600 nm × 600 nm; 1024 pixels × 1024 pixels). Baseline subtraction, contact point determination and vertical tip position calibration were performed for each force curve. The region of the force curve from minimal force to 50% of the setpoint force was fitted by the Hertz model to determine the compressive Young's modulus. Fifty force curves on mica were processed to calibrate the cantilever sensitivity. The spring constant of the cantilever was calibrated using the thermal noise method.

Mass photometry assays

The mass photometry experiment was carried out on a Refeyn TwoMP mass photometer at room temperature. Glass coverslips (18 mm × 18 mm, VWR) were cleaned by bath sonication in Milli-Q water for 5 min, isopropanol for 5 min and Milli-Q water again for 5 min. Sample carrier slides (Refevn) were washed thoroughly in Milli-O water, isopropanol and Milli-Q water again. Both coverslips and slides were dried using a nitrogen stream. Double-sided tape was used to attach the glass coverslip on the slide to make a flow chamber. Standard samples including bovine serum albumin (66 kDa) and β-amylase (110 kDa) were measured to obtain the calibration curve. Solution was added by pipette on one end of the flow chamber, and filter paper was used on the other end to absorb excess solution. The detection concentration of VIPP1 was 0.6 μM. VIPP1 equilibrated at 2 μM was diluted to 0.6 μM by imaging buffer and measured immediately. The events were read out using the software Refeyn DiscoveryMP. The molecular mass of the particles was obtained by comparison with the calibration curve.

Data analysis

HS-AFM data were saved as tiff stacks. HS-AFM videos were flattened and aligned using in-lab video flattener and video aligner plugins in ImageJ, respectively. For the HS-AFM images in the figures, a singular value decomposition algorithm was applied further to calibrate non-linearly fluctuating background. The Otsu thresholding algorithm was applied to segment images, unless otherwise specified. Data and images were processed using Python scripts and ImageJ or Fiji.

Surface coverage ratio measurement. Each flattened image frame in $7 \mu m \times 7 \mu m$ HS-AFM measurements was segmented into the SLB layer and the protein layer. The coverage ratio of each frame was calculated as

the ratio of the protein layer area of the total area. Coverage ratio curves of parallel measurements were averaged after curves were aligned to the point of coverage ratio = 0.5.

Curvature measurement. The curvature of filaments was measured by the plugin Kappa in Fiji. First, the images were converted to 8-bit so that the pixel values ranged from 0 to 255. Next the image was imported to the Kappa plugin, in which the parameter scale was set according to the image, the threshold was set to 50 and data threshold radius was set to 2. Then the curvature and corresponding coordinates of filaments were read from the measurement. The height was read from original images according to the coordinates.

Persistence length and thickness measurement. Freely fluctuating filaments in HS-AFM images were segmented by height. The filament contour length was measured by segmented lines in ImageJ. The average thickness of the filament was calculated from the filament area divided by the contour length. The persistence length was calculated by the expression³³:

$$\ell_p = \frac{\sum_n e^{i\theta_n} s_n \Delta s_n}{\sum_n e^{i\theta_n} \Delta s_n}$$

where θ_n is the slope angle of the segmented line, Δs_n is the length of the segmented line and $s_n = \sum_{i=1}^n \Delta s_i$. The data were fitted by the elastic rod model, in which the persistence length ℓ_p satisfies the expression⁵²:

$$\ell_p = \frac{Yhw^3}{12k_BT},$$

where Y is the Young's modulus, h is the height of the filament, w is the thickness of the filament and k_BT is the thermal energy.

Polygon analysis. First, videos were projected into one frame using the median filter along the taxis to reduce noise. The local thresholding Niblack algorithm was applied, and the mask was pruned manually to get well-separated protein layers and striation layers. To estimate the number and angle of the intersector boundaries, the mask was divided into four parts: top left, top right, bottom left and bottom right. Subsequently, the Hough transform was applied to each part of the mask. As a result, the straight lines in the mask are transferred to local maxima in Hough space, and the number and angle of intersector boundaries are obtained from the number and coordinates of the local maxima in Hough space, respectively. A degree of freedom of n-1 was used, in which n is the number of boundaries. To measure the equivalent radius, we segmented the center from the other surface of polygons by the hysteresis thresholding algorithm, in which the high threshold of the algorithm is 0.8 multiplied by the maximum of the center and the low threshold is 1.1 multiplied by the median of the polygons outside the center. The consequent segmentation was pruned manually if needed.

Growth analysis. First, each frame of the raw videos was labeled using integers as time stamps. Then, some frames were removed, during which the AFM tip detached from the surface or the sample stage was unstable. Only isolated VIPP1 polymers were selected for analysis (Supplementary Video 2). For spirals, the hysteresis thresholding algorithm with higher and lower thresholds of 10 pixels and 20 pixels, corresponding to $5.4\times10^{-3}~\mu\text{m}^2$ and $1.08\times10^{-2}~\mu\text{m}^2$, was applied to the area–time growth curves to separate the nucleation state and growth stages, which can further be divided into fast-growing and slow-growing stages. Growth curves were aligned on the transition point between the nucleation stage and the fast growth stage. For polygons, we approximated the polygon as a circle using the equation:

$$4\pi A = P^2$$
.

where *P* and *A* are the perimeter and the area of the polygon, respectively. Taking the derivative with respect to time *t* on both sides of the above equation yields:

$$\dot{A} = \dot{r} \times P$$
,

where r is the radius of the polygon. The data for \dot{A} and P were fitted by a linear model with the slope $\dot{r}=1.1\pm0.1~{\rm nm\,s^{-1}}$. To further interpret this fit, we assumed that the polymerization of VIPP1 was diffusion-controlled, in which case the area of a single VIPP1 filament ($A_{\rm ss}$) should depend linearly on the time t:

$$A_{\rm ss} = \alpha \times t$$

where α is the association rate of VIPP1 filaments. Therefore, the polygon area A_{ms} along which multiple VIPP1 filaments assemble is given by:

$$A_{\rm ms} = k \times \alpha \times t$$
,

where k is the number of growing filaments along the polygon periphery, which we take to follow a Poisson distribution. Because the SASA relevant for polygon polymerization should be proportional to the polygon perimeter, we can thus obtain the average of $A_{\rm ms}$:

$$< A_{\rm ms} > = < k > \times \alpha \times t = \lambda P \alpha t,$$

where λ is the number of growing filaments along the unit perimeter. The above equation can be recast in terms of the polygon radius r:

$$r = 2\lambda \alpha t$$
.

The linear growth model with a constant slope $\dot{r}=1.1\pm0.1$ nm s⁻¹ is therefore consistent with a growth model in which multiple VIPP1 filaments assemble along the periphery of polygons.

Boundary distance determination. The centroid of the spirals was determined from the first five frames and identified as the nucleation site. Subsequently, the nucleation site was used as the origin to align the local segmentations of spirals, which enabled us to obtain boundary profiles of spirals at different times and, thus, the growth velocity at all angles. Then, the distance from the nucleation site to the segmentation boundary and corresponding angles were obtained by converting the boundary profiles into the polar coordinate system. The distance distribution was obtained by aligning the fastest growing direction of spirals to the angle 180° as a function of time and angle. Spirals were simulated on the basis of the logarithmic spiral model with the fitted values $r_0 = 45.5$ nm and k = 0.041.

Filament flow measurement (angular velocity analysis). The thickness and radius of curvature of each filament were measured manually every ten HS-AFM Video frames in ImageJ. In every frame, regions corresponding to individual filaments were labeled manually in ImageJ. The regions were computationally straightened and projected along the width by max filter to get a $1 \times n$ pixels line, which was concatenated with other lines obtained from different frames to form the kymographs. The filament velocities were obtained from these kymographs. The angular velocities were calculated by dividing the filament velocities by the radius. See Extended Data Figure 8 for more details.

Monte Carlo simulation

Spiral growth was simulated by the lattice Monte Carlo method with longitudinal and lateral subunit binding. First, one subunit with

intrinsic curvature c_0 is bound by another subunit laterally or longitudinally, thus forming the nucleation site. Lateral binding introduces a new strand into the filament and thus thickens the filament. Meanwhile longitudinal binding elongates the filament. The curvature at each site was determined by averaging over the local curvatures of its neighboring sites. These local curvatures were obtained from the thickness at each site according to the fitted logarithmic spiral model. On the basis of the curvatures, we generated the geometric structure of the spiral, for which the bending energy was calculated by the ESCRT-III mechanical rules Finally, the statistically correct trajectories of reactions were generated according to the Gillespie algorithm More details can be found in Supplementary Note 3.

Statistics and reproducibility

HS-AFM imaging. Imaging of the polymerization process from 2 μM VIPP1 bulk concentration on 50% DOPC:50% DOPS SLBs was performed more than 10 times. Eight measurements at 0.125 frames s $^{-1}$ were used for analysis. The same measurements at varying VIPP1 concentrations (0.5 μM, 1.25 μM, 2.5 μM, 3.5 μM and 5 μM) or SLB DOPC:DOPS ratios (0%, 25%, 50%, 63%, 75% and 100% DOPS) were performed once. Concentration gradients were made by sequential dilution to ensure comparability. The periodical striations on spirals and polygons could be observed repeatedly with pixel sampling below 1 nm per pixel. Force-sweep experiments were performed more than five times each on spirals and polygons. Measurements were performed from three individually purified protein batches.

AFM nanomechanical mapping. Measurements were performed more than 3 times.

Mass Photometry. Measurements were performed more than 3 times.

Reporting summary

Further information on research design is available in the Nature Portfolio Reporting Summary linked to this article.

Data availability

The manuscript figures, supplementary figures, and supplementary Videos contain all data necessary to interpret, verify and extend the presented work. Raw HS-AFM, nanomechanical mapping and mass photometry data are available on GitHub (https://github.com/psichen/VIPP1-polymerization-analysis). The raw data files can be obtained from the authors upon reasonable request. Source data are provided with this paper.

Code availability

 $Codes \, used \, for \, HS-AFM \, analysis \, and \, simulation \, are \, available \, on \, Git Hub \, (https://github.com/psichen/VIPP1-polymerization-analysis).$

References

- 52. Landau, L. D., Lifšic, E. M., Lifshitz, E. M., Kosevich, A. M. & Pitaevskii, L. P. *Theory of Elasticity* Vol. 7 (Elsevier, 1986).
- Meadowcroft, B. et al. Mechanochemical rules for shape-shifting filaments that remodel membranes. *Phys. Rev. Lett.* 129, 268101 (2022).

Acknowledgements

Work in the Scheuring laboratory was supported by grants from the National Institute of Health (NIH), National Center for Complementary and Integrative Health (NCCIH), DP1ATO10874 and National Institute of Neurological Disorders and Stroke (NINDS), R01NS110790. Work in the Schroda laboratory was supported by the Deutsche Forschungsgemeinschaft, TRR175, project C02. The Engel laboratory was supported by ERC consolidator grant 'cryOcean' (fulfilled by the Swiss State Secretariat for Education, Research and Innovation, M822.00045). Work in the Haselwandter group was supported by the National Science Foundation (NSF) through grant no. DMR-2051681.

Author contributions

S.P., B.D.E., M.S. and S.S. designed the study; S.P. performed HS-AFM and AFM mechanical mapping experiments, mass photometry experiments and simulations; K.G. produced the recombinant VIPP1 protein and was supervised by M.S.; C.A.H. developed the physical model of VIPP1 filament organization; S.P. and S.S. analyzed data and wrote the paper with contributions from C.A.H., M.S. and B.D.E.; S.S. supervised the project.

Competing interests

The authors declare no competing interests.

Additional information

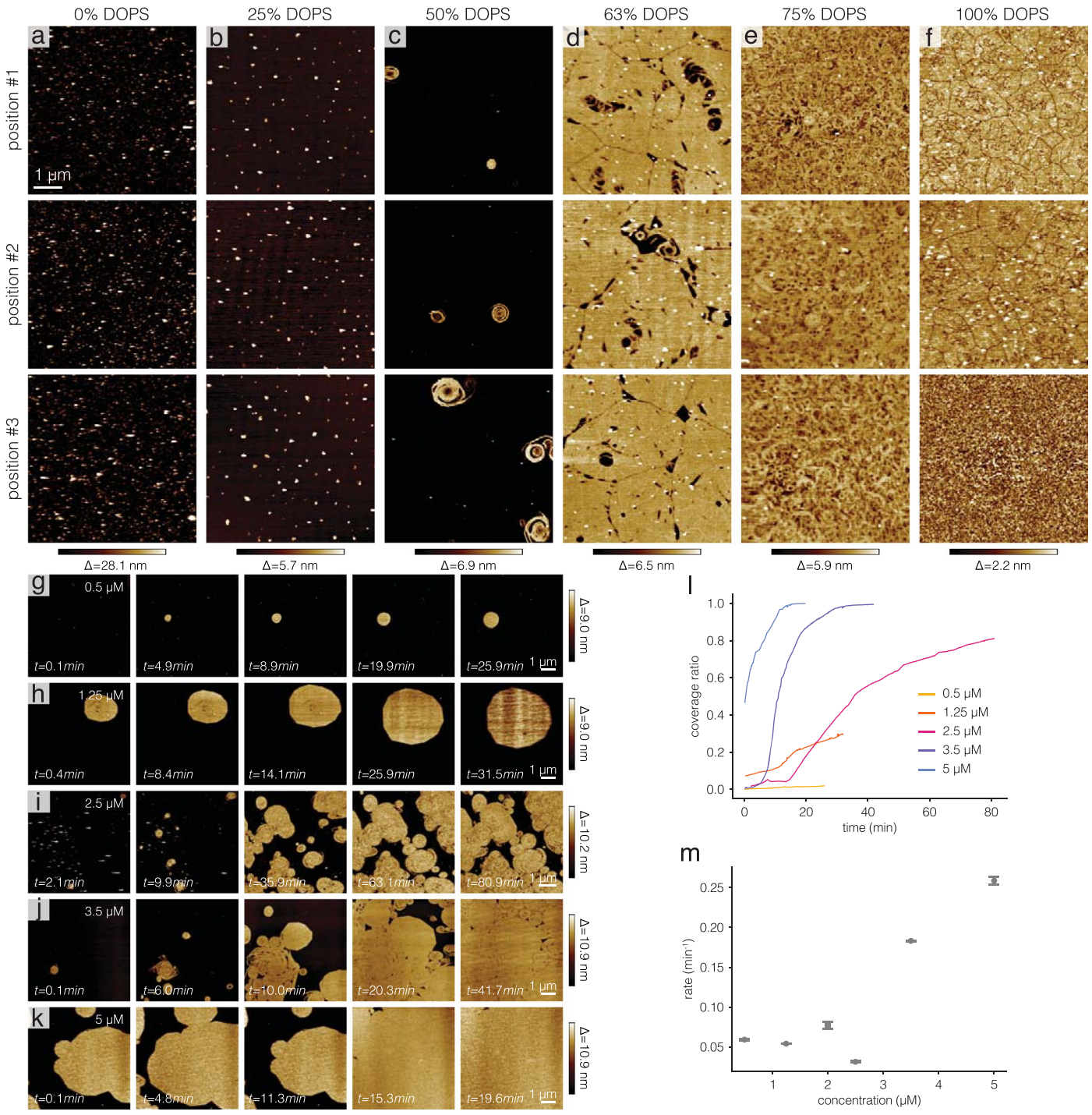
Extended data is available for this paper at https://doi.org/10.1038/s41594-024-01367-7.

Supplementary information The online version contains supplementary material available at https://doi.org/10.1038/s41594-024-01367-7.

Correspondence and requests for materials should be addressed to Simon Scheuring.

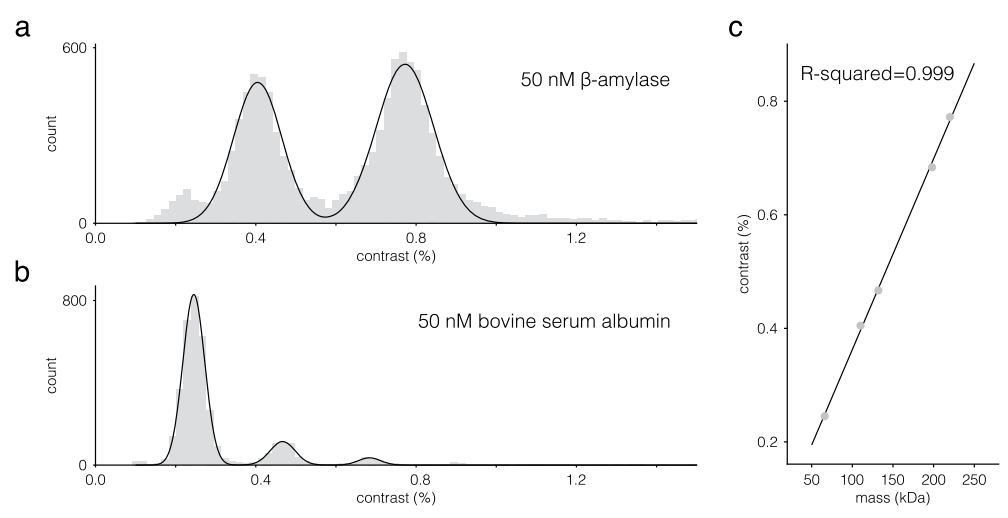
Peer review information Nature Structural & Molecular Biology thanks Georg Fantner, Alice Pyne, Roger Williams and the other, anonymous, reviewer(s) for their contribution to the peer review of this work. Primary Handling Editor: Katarzyna Ciazynska, in collaboration with the Nature Structural & Molecular Biology team. Peer reviewer reports are available.

Reprints and permissions information is available at www.nature.com/reprints.



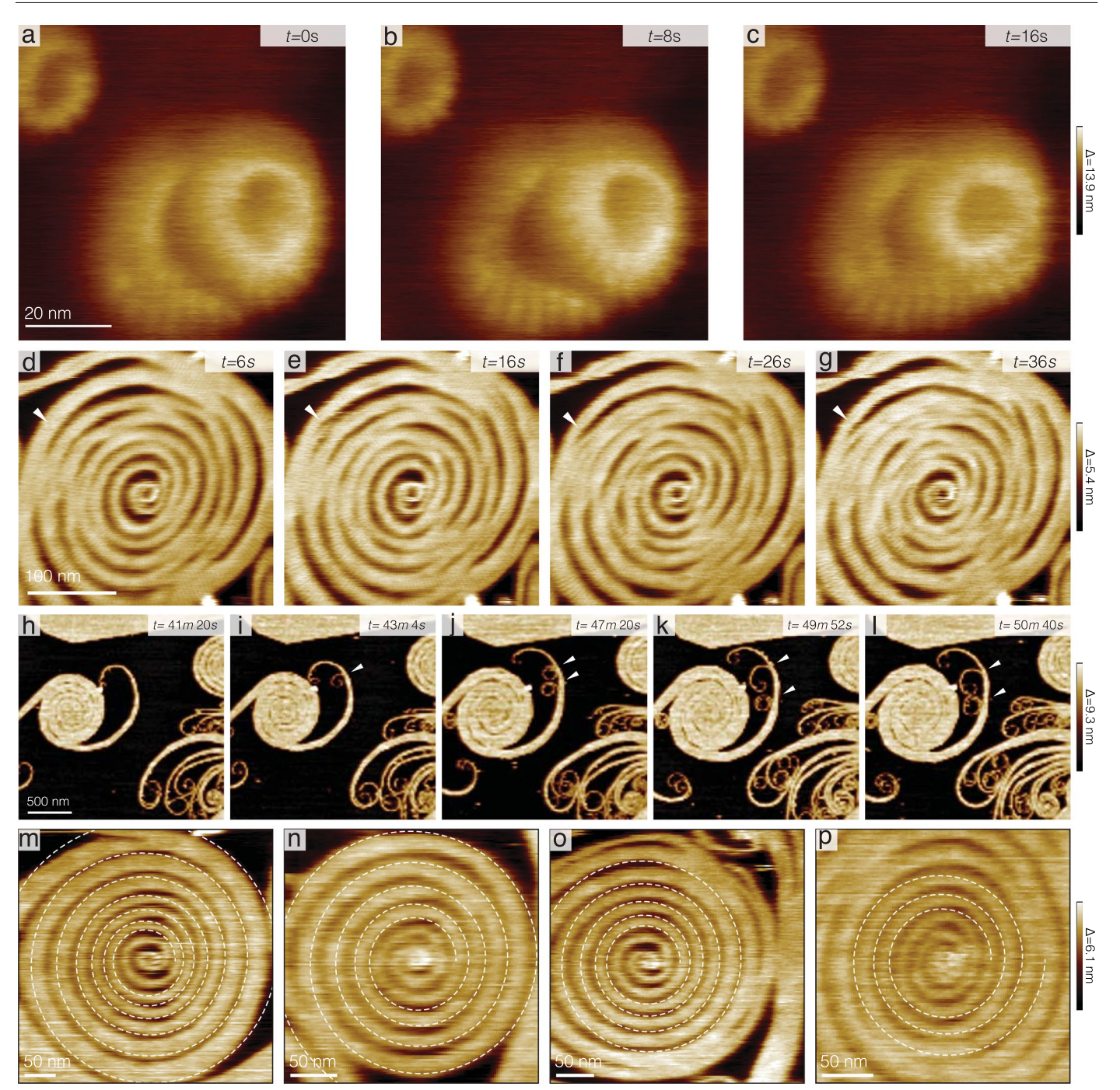
Extended Data Fig. 1 | VIPP1 polymerization from solutions at varying VIPP1 bulk concentrations and on SLBs of varying DOPS:DOPC ratios. (a-f) VIPP1 (4 μ M) polymerization on SLBs composed of 0% DOPS, 25% DOPS, 50% DOPS, 63%. DOPS, 75% DOPS and 100% DOPS. VIPP1 polymers are only formed on SLBs containing >50% DOPS. When VIPP1 forms patches, the patch area decreases at higher DOPS ratios (63% DOPS, 75% DOPS, and 100% DOPS), suggesting that DOPS facilitates nucleation of VIPP1 polymers. (g-k) VIPP1 polymerized on

SLBs from $0.5\,\mu\text{M}$, $1.25\,\mu\text{M}$, $2.5\,\mu\text{M}$, $3.5\,\mu\text{M}$, and $5\,\mu\text{M}$ VIPP1 bulk concentration. (I) VIPP1 surface coverage ratio curves on DOPC:DOPS (1:1) SLBs. Coverage ratio curves were fitted by logistic regression to estimate growth rates. (m) Estimation of VIPP1 concentration-dependent polymerization kinetics. Growth rate (dots) increased with increased VIPP1 concentration (n = 1, respectively). The growth rate at 2 μ M in Fig. 1j in the main text is shown as a square (n = 8). Data are presented as fitted value \pm fitting errors.



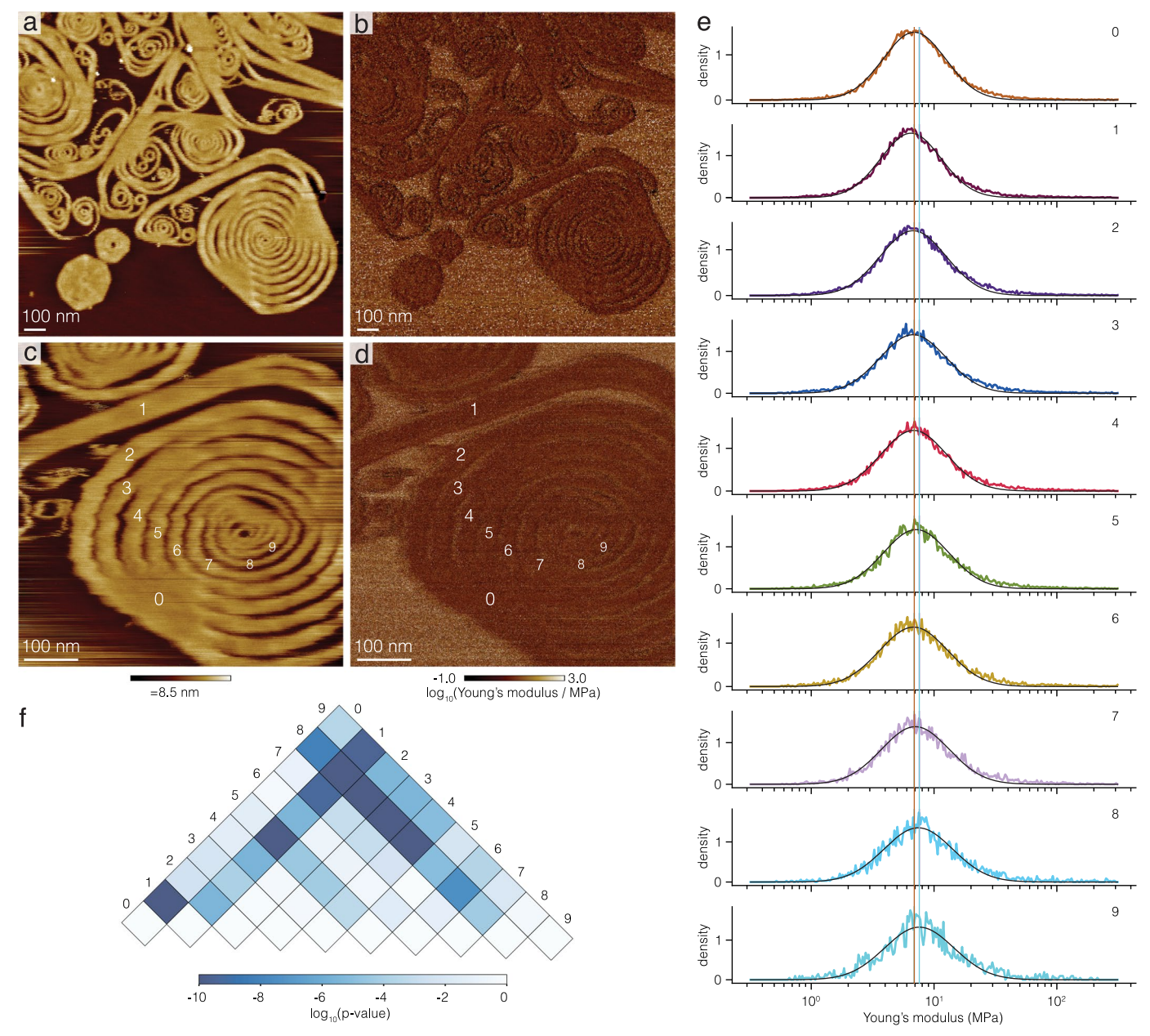
Extended Data Fig. 2 | **Calibration of mass photometry.** The contrast histograms of (a) β -amylase and (b) bovine serum albumin were fitted by Gaussian distributions to obtain contrast values of the corresponding oligomers

(β -amylase monomer: 110 kDa; dimer: 220 kDa; bovine serum albumin monomer: 66 kDa; dimer: 132 kDa; trimer: 198 kDa). (c) The calibration curve was obtained by linear fitting between mass and contrast with R-squared=0.999.



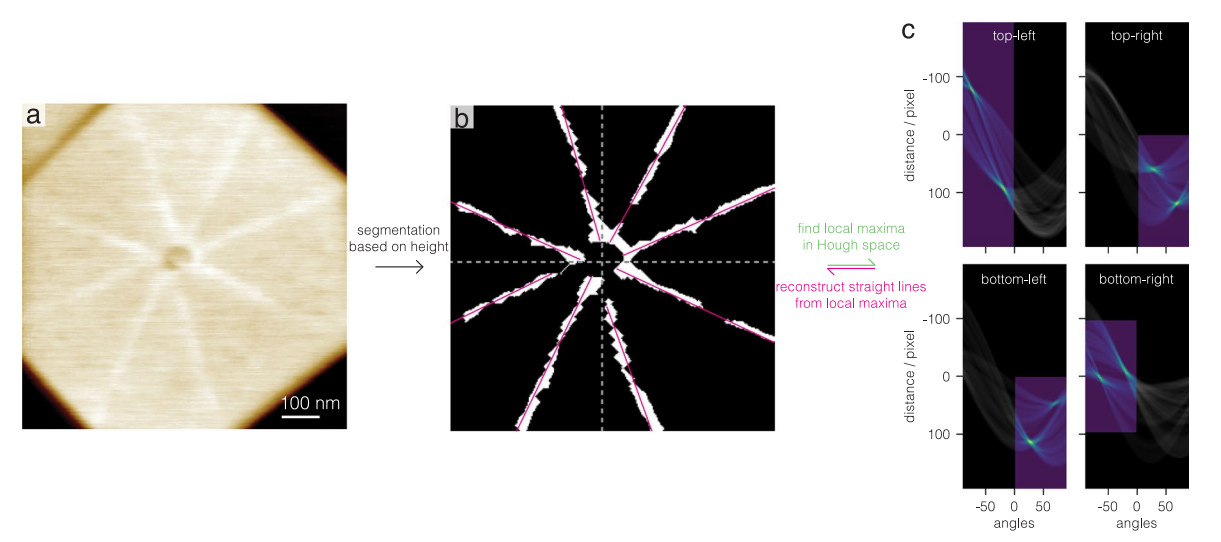
Extended Data Fig. 3 | VIPP1 filament preferred curvature and dynamics is filament thickness-dependent. (a-c) The stacked VIPP1 ring structure on a SLB at 0 s, 8 s and 16 s. Minor changes in the gap structure between rings and in the periodic structure within the top ring can be observed. We hypothesize that these slightly stacked ring structures represent the ring-shaped polymerization hub at the center of spirals and polygons. (d-g) HS-AFM images of the VIPP1 spiral at 6 s, 16 s, 26 s and 36 s. A VIPP1 strand is seen to dissociate and associate with adjacent filaments. The dissociation and association sites are indicated by white triangles.

(h-1) Thin VIPP1 filaments dissociate from existing thick filaments and form smaller spirals spontaneously (white triangles), demonstrating a higher preferred curvature for thinner filaments. (**m-p**) The gap between filaments was fitted by the logarithmic spiral equation $r = r_0 \exp(k\theta)$, which yielded average fit values $r_0 = 45.5$ nm and k = 0.041. Thus, the thickness of filaments t_f and the radius of curvature of filaments r_f were derived as $t_f = 2 \cdot (1 - \exp(-2\pi k)) / (1 + \exp(-2\pi k)) \cdot r_f$, which was linear.



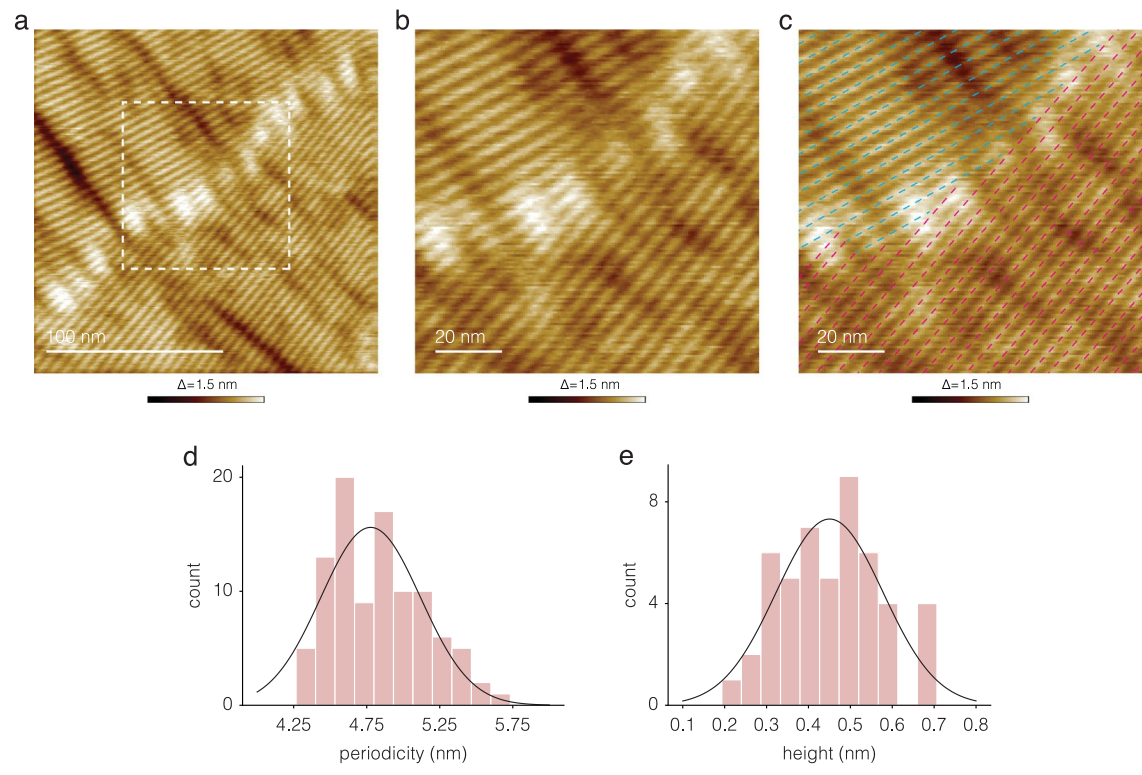
Extended Data Fig. 4 | Mechanical properties of VIPP1 spirals. (a and c) Topography height maps, and (b and d) corresponding Young's modulus maps of VIPP1 spirals. (e) Elasticity distributions of VIPP1 spiral turns as labeled in (c) and (d). Young's moduli have wide distributions with a slight increase of the mean value in the more central spiral turns. The mean values associated with

the distributions labeled by 0 and 9 are shown by brown and cyan vertical lines, respectively. (f) p-values are calculated among Young's modulus distributions according to the two-sided t-test, which shows significant differences between the Young's moduli of inner and outer spiral turns.



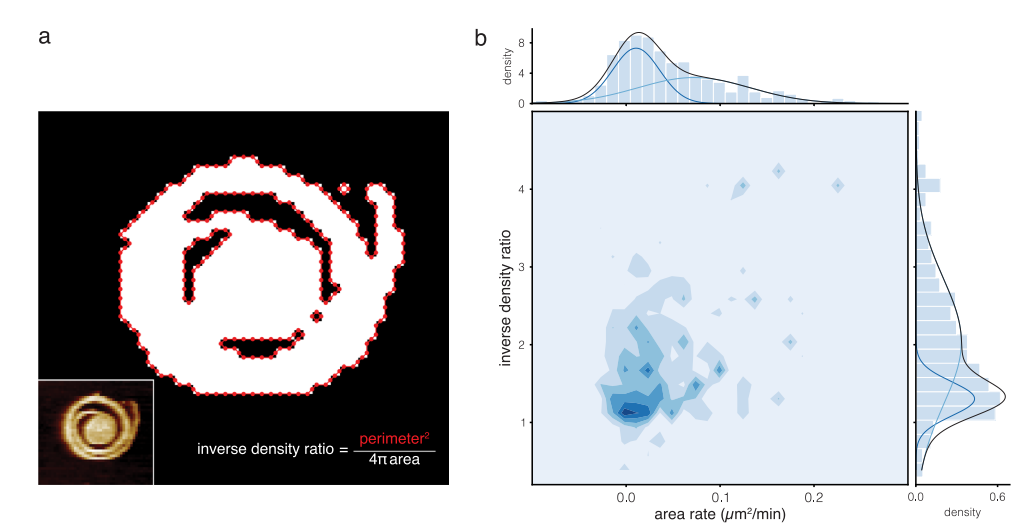
Extended Data Fig. 5 | Workflow for the estimation of striations by Hough transforms. (a) A VIPP1 polygon with 8 inter-sector boundaries. (b) The image in (a) was segmented and pruned manually to find the pixels of striations. The pixels were divided into 4 parts separated by grey dashed lines for further Hough transform. (c) The pixels in 4 regions were transformed to Hough space. Because

inter-sector boundaries in 4 corners only adopted angles in a certain range, the corresponding local maxima were searched only in particular regions, which were represented by light regions in Hough space. The coordinates of the local maxima allow reconstruction of the straight red lines in (b).



Extended Data Fig. 6 | Detailed structure of VIPP1 polygons. (a) HS-AFM image showing an inter-sector boundary and the subunit periodicity in the neighboring sectors of a VIPP1 polygon. **(b)** Enlarged region of the HS-AFM image outlined by the dashed boxed region in (a). **(c)** Subunit periodicities

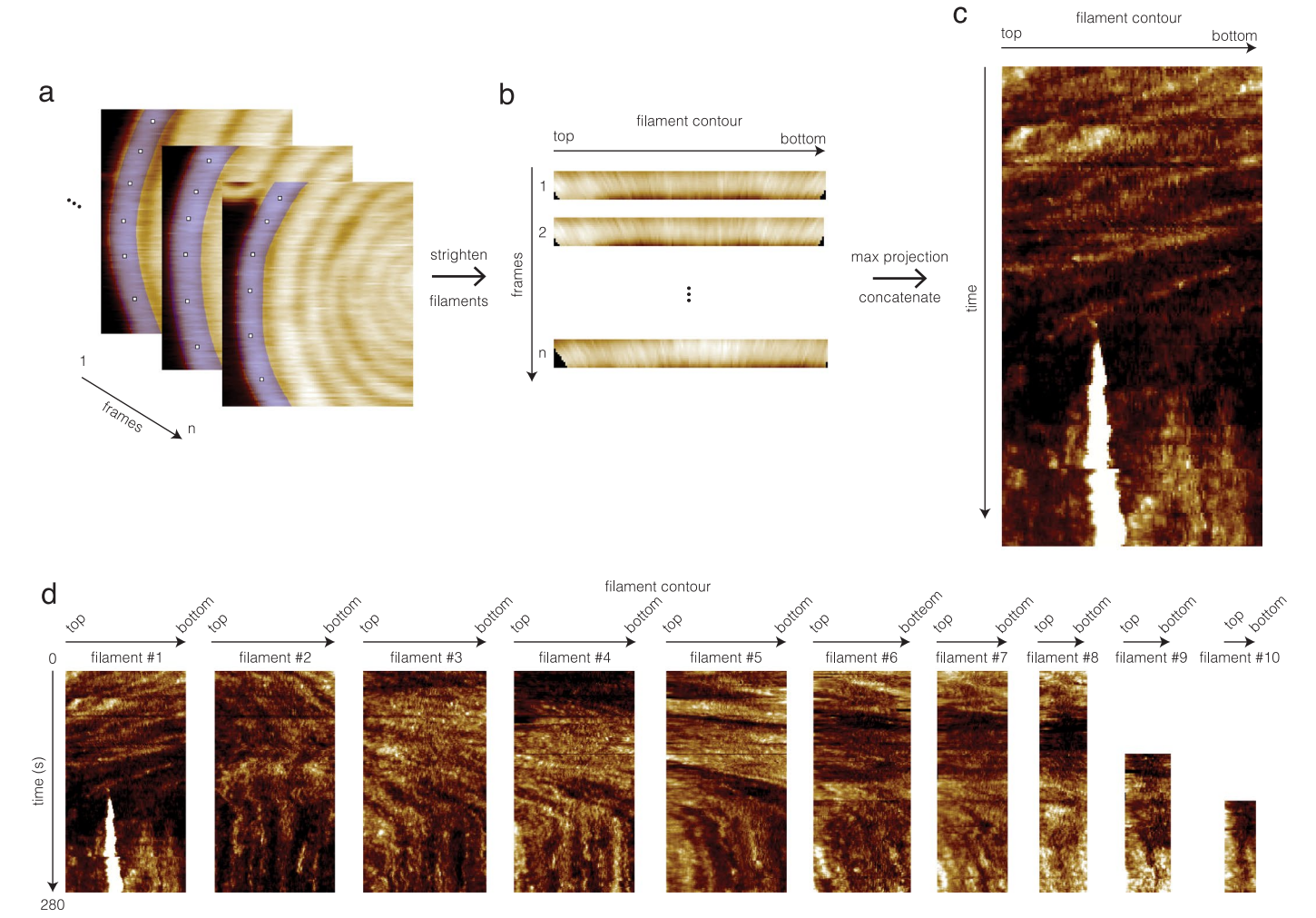
on each side of the inter-sector boundary display directional discontinuity. (**d**) Distribution of subunit periodicity. (**e**) Distribution of inter-sector boundary height above the mean height of sectors. Distributions were fitted by Gaussians.



Extended Data Fig. 7 | Spiral densification slows spiral growth rate.

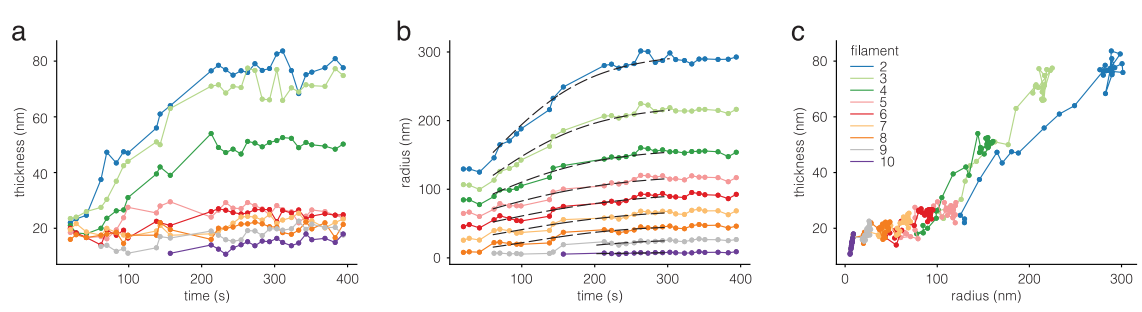
(a) Estimation of the extent of spiral compactness. The perimeter of a segmented spiral is shown in red. When a spiral is compact, the spiral shape is close to a circle and the inverse density ratio is close to 1. Otherwise, the inverse density ratio is greater than 1. Inset: Original HS-AFM image of the VIPP1 spiral. (b) The joint

distribution of area expansion rate and inverse density ratio shows a positive correlation, suggesting that the spiral self-densification interferes with spiral growth. The margin distributions of area growth rate and inverse density ratio were fitted by two Gaussian distributions, respectively.



Extended Data Fig. 8 | **Filaments in spirals showed varying angular velocities during the spiral growth process.** $(\mathbf{a}-\mathbf{c})$ The workflow for generating the kymograph of moving trajectories (a) The selected filament was masked manually to identify the regions of interest (ROIs) in every frame. (b) The ROI in every frame was straightened so as to obtain a rectangular shape. (\mathbf{c}) Every ROI was projected by max filter along the width to a $1 \times n$ pixels line in which n is the pixel number of the filament contour. Then the resulting lines were concatenated on the frame dimension to construct the kymograph. The vertical lines in the

kymograph represent the moving trajectories of bright spots on filaments, from which the filament velocities were calculated. The radius in every frame was obtained by the logistic regression in Extended Data Fig. 9b. (\mathbf{d}) Each filament was straightened and projected to a line with width of one pixel. Lines at different times were concatenated along the strand thickness dimension to form the moving trajectories of bright spots on the filament. From the angular velocity the filament 'flow' could be directly calculated.



Extended Data Fig. 9 | Measured spiral filament thickness and radius of curvature as a function of time. (a) Filament thickness as a function of time. (b) Filament radius as a function of time. Black lines: Logistic regression of each filament. The thickness and radius of outer filaments increased rapidly

and eventually reached a plateau. In contrast, the thickness and radius of inner filaments only showed slight changes. (c) Filament thickness as a function of radius. The thickness was nearly linearly correlated with the radius. All curves were colored as in main text Fig. 5e.

nature structural & molecular biology

Supplementary information

https://doi.org/10.1038/s41594-024-01367-7

The cyanobacterial protein VIPP1 forms ESCRT-III-like structures on lipid bilayers

In the format provided by the authors and unedited

Table of contents

Supplementary Note 1	2
Supplementary Note 2	5
VIPP1 logarithmic spiral model	5
VIPP1 dynamic logarithmic spiral model	6
Supplementary Note 3	
Simulation procedure	8
Energy calculation	9
Calculating the rates of binding and unbinding	10
Generation of spiral coordinates	10

Supplementary Note 1: Analytic model of the competition between spiral and polygonal VIPP1 organization

We develop here a simplified analytic model of VIPP1 organization that aims to capture the competition between VIPP1 filament bending energies, lateral binding energies, and grain boundary energies in spiral and polygonal VIPP1 assemblies. For simplicity, we neglect the pitch or detailed organization of spiral structures and, instead, consider closed filament strands of length $2\pi R$. Specifically, we ask: Is it energetically more favorable for a given VIPP1 filament strand of length $2\pi R$ to take the shape of a circle or the shape of a regular polygon with symmetry n (Supplementary Figure 1a)? We thus aim to understand and predict the observed faceting of (logarithmic) spirals into polygonal shapes.

We denote the energy of polygonal filament strands by $G_p(R, n)$ and the energy of circular filament strands by $G_c(R, n)$. We assume that $G_p(R, n)$ is dominated by three distinct contributions.

First, experiments indicate lateral ordering of VIPP1 within individual polygonal sectors. Hence, we expect there to be a favorable lateral binding energy of VIPP1 in polygons that, for a given strand, is proportional to the length of the strand, resulting in a term $-2\pi R\epsilon$ in $G_p(R,n)$, where $\epsilon > 0$ is the effective lateral binding energy per unit length.

Second, experiments demonstrate grain boundaries between adjacent polygonal sectors, which we expect to introduce an energy cost. For simplicity, we assume that this energy cost does not depend on the polygonal symmetry, yielding a term $n\delta$ in $G_p(R,n)$, where $\delta > 0$ is the energy cost associated with each vertex of a regular n-gon. Note, that, since the vertex angles of polygons are independent of polygon size, δ is—at least to a first approximation—not expected to depend on R. Moreover, as discussed in the main text, it is found in experiments that $n \geq 8$, which suggests that VIPP1 may only be able to accommodate polygons with large enough internal angles. We therefore focus here on regular polygons with $n \geq 8$.

Finally, third, polygonal VIPP1 strands are approximately straight along the polygon sides while VIPP1 strands are expected to have a preferred, nonzero curvature, resulting in a nonzero bending energy of polygonal strands. We therefore allow for a bending energy term $2\pi R \frac{\kappa}{2R_0^2}$ in $G_p(R, n)$, where $\kappa > 0$ and $R_0 > 0$

0 are the flexural rigidity and the preferred radius of curvature of VIPP1 filament strands, respectively. Based on the experiments described in the main text we expect that R_0 sets the lower bound on R, $R \ge R_0$. Combining these three distinct contributions to $G_p(R, n)$ we arrive at

$$G_p(R,n) = -2\pi\epsilon R + n\delta + \frac{\pi\kappa}{R_0^2}R.$$
 (1)

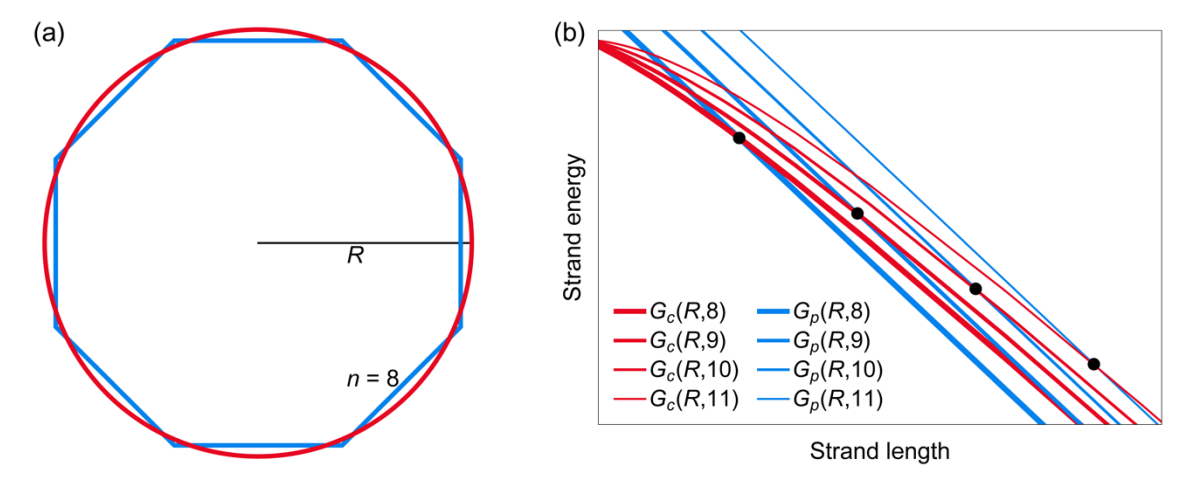
We construct the energy of circular filament strands, $G_c(R,n)$, following similar steps as for Eq. (1). In particular, by analogy to Eq. (1) we have a bending energy term $2\pi R \frac{\kappa}{2} \left(\frac{1}{R} - \frac{1}{R_0}\right)^2$ for circular filament strands of radius R. Moreover, for self-consistency we demand that $G_c(R,n)$ and $G_p(R,n)$ become equal to each other as $R \to \infty$ since, in this limit, the filament strands are always straight. We therefore take $G_c(R,n)$ to be of the form,

$$G_c(R,n) = \pi \kappa R \left(\frac{1}{R} - \frac{1}{R_0}\right)^2 + \left(-2\pi \epsilon R + n\delta\right) \left(1 - \frac{R_0}{R}\right),\tag{2}$$

where the second term ensures that $G_c(R,n) \to G_p(R,n)$ as $R \to \infty$. As in Eq. (1), the term $(-2\pi\epsilon R + n\delta)$ in Eq. (2) captures contributions to $G_c(R,n)$ due to VIPP1 lateral ordering and disruptions of longitudinal VIPP1 binding. This term is multiplied by the term $\left(1 - \frac{R_0}{R}\right)$ in Eq. (2) so that $\left(-2\pi\epsilon R + n\delta\right)$ does not contribute to $G_c(R,n)$ at $R = R_0$, and so that the contribution $\left(-2\pi\epsilon R + n\delta\right)$ to $G_c(R,n)$ decreases linearly with the curvature of circular filament strands. At the cost of introducing additional model parameters or model

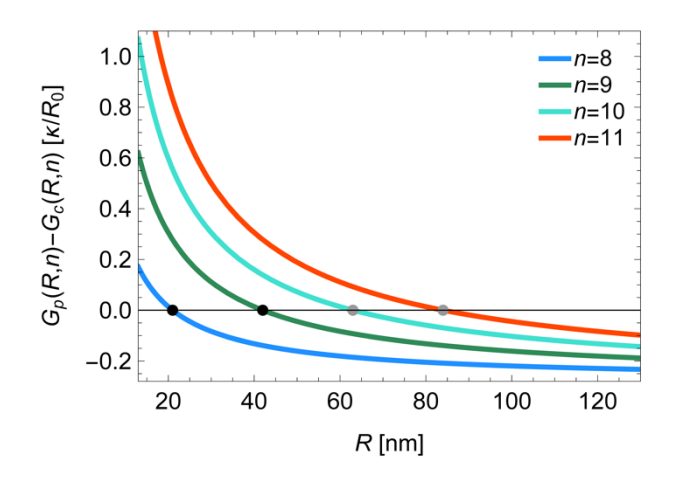
Pan et al., 2024 Page 2 of 11

assumptions, more intricate mathematical descriptions of how $G_c(R, n)$ approaches $G_p(R, n)$ as $R \to \infty$ could be considered in Eq. (2).



Supplementary Figure 1 | Energy of circular and polygonal filament strands. (a) We consider in our physical model of VIPP1 organization the energy difference between circular (red curve) and regular polygonal (blue curve) filament strands with the same total length, $2\pi R$. We denote the symmetry of polygons by n. (b) For large enough values of ϵ and δ in Eqs. (1) and (2) our model of VIPP1 organization favors circular filament strands at small R [$G_c(R,n) < G_p(R,n)$] and polygonal filament strands at large R [$G_c(R,n) > G_p(R,n)$], with transitions to regular n-gons with larger n being associated with larger values of R. Values of R for which $G_c = G_p$ at a given n, $R = R_c$, are marked by black dots along each curve.

Equations (1) and (2) allow us to examine the competition between polygonal and circular shapes of VIPP1 filament strands. In particular, circular filament strands are stable (energetically favorable) in our model if $G_c(R,n) < G_p(R,n)$ but are expected to facet into polygonal shapes if $G_c(R,n) > G_p(R,n)$. For a large enough lateral binding energy of VIPP1 filament strands and a large enough penalty for grain boundaries along polygonal sectors—*i.e.*, large enough values of ϵ and δ in Eqs. (1) and (2)—Eqs. (1) and (2) have the feature that circular filament strands are favorable at small R, with filament strands faceting into polygonal shapes at large R (Supplementary Figure 1b). This generic prediction of Eqs. (1) and (2) is consistent with the experimental observations on VIPP1 filaments described in the main text. Furthermore, Eqs. (1) and (2) imply that regular polygons with larger n only become favorable at larger values of R, which is also consistent with experimental observations (see Figure 3d in the main text). Thus, the model of VIPP1 organization in Eqs. (1) and (2) allows us to understand how the competition between VIPP1 filament bending energies, lateral binding energies, and grain boundary energies can produce transitions between spiral and polygonal VIPP1 assemblies as a function of R and n.



Supplementary Figure 2 | Predicting the transition between spiral and polygonal VIPP1 assemblies. Difference between $G_p(R,n)$ in Eq. (1) and $G_c(R,n)$ in Eq. (2) as a function of R for n=8,9,10, and 11. To plot these curves, we first solved for ϵ and δ in terms of κ and R_0 using the values of R_c measured for n=8 and 9 (black dots), which then allows prediction of R_c via Eq. (3) for n=10 and 11 (gray dots). We set $R_0=13$ nm, and plot $G_n(R,n)-G_c(R,n)$ in units of κ/R_0 .

Pan et al., 2024 Page 3 of 11

Beyond the qualitative features of our model of VIPP1 organization summarized in Supplementary Figure 1b, we can use Eqs. (1) and (2) to make quantitative predictions that can be compared directly with experimental observations. To this end, we solve for the critical value of R, $R = R_c$, for which G_p and G_c in Eqs. (1) and (2) are equal to each other,

$$R_c(n) = \frac{(n\delta R_0 - \pi \kappa)R_0}{2\pi(\epsilon R_0^2 - \kappa)}.$$
 (3)

Figure 3d in the main text provides experimental estimates of R_c for $n=8,\,9,\,10$, and 11. In particular, Figure 3d in the main text implies that $R_c\approx 21$ nm and $R_c\approx 42$ nm for n=8 and n=9, respectively, which correspond to dominant polygonal symmetries. We substitute these two values of R_c into Eq. (3) to solve for ϵ and δ in terms of κ and R_0 . Substituting, in turn, the resulting expressions for ϵ and δ into Eq. (3) we thus predict, with no adjustable parameters, that $R_c\approx 63$ nm and $R_c\approx 84$ nm for n=10 and n=11, respectively. The corresponding experimental estimates in Figure 3d in the main text are $R_c\approx 60$ nm and $R_c\approx 92$ nm for n=10 and n=11, respectively. Considering the simplicity of the model employed here, and uncertainties inherent in the experimental results in Figure 3d in the main text, the agreement between experimental estimates of the critical (equivalent) radius R_c and the corresponding predictions implied by Eqs. (1) and (2) appears to be rather good.

Supplementary Figure 2 shows the difference between $G_p(R,n)$ in Eq. (1) and $G_c(R,n)$ in Eq. (2) as a function of R for n=8,9,10, and 11. We thereby used the expressions for ϵ and δ implied, as described above, by experimental observations on R_c for n=8 and n=9 (black dots in Supplementary Figure 2). Furthermore, from Figure 2b in the main text we estimate $R_0=13$ nm for the preferred radius of curvature of VIPP1 filament strands. As described above, the values of R_c associated with $G_p=G_c$ for n=10 and 11, which are marked by gray dots in Supplementary Figure 2, represent model predictions. As expected from the qualitative behavior of Eqs. (1) and (2) sketched in Supplementary Figure 1b, we find in Supplementary Figure 2 that $G_c < G_p$ for small strand radii R but $G_c > G_p$ for large enough R, with the value of R separating these two regimes, $R=R_c$, increasing with increasing R. Thus, our model of VIPP1 organization in Eqs. (1) and (2) captures and explains key qualitative and quantitative features of the observed faceting of (logarithmic) spirals into regular polygons.

Pan et al., 2024 Page 4 of 11

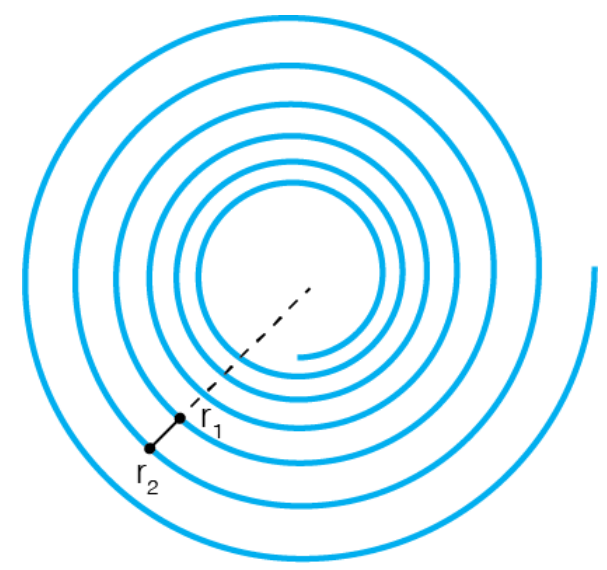
Supplementary Note 2: VIPP1 forms dynamic logarithmic spirals

VIPP1 logarithmic spiral model

As shown in Extended Data Figure 3m-p and in the manuscript, the gap between VIPP1 spiral filaments can be fitted by a logarithmic spiral model (**Supplementary Figure 3**),

$$r = r_0 \exp(k\theta)$$
,

where r is the radius of curvature of gap trajectories, r_0 is the initial radius, k is the scale parameter, and θ is the angle.



Supplementary Figure 3 | **VIPP1 logarithmic spiral model.** The logarithmic spiral (blue) represents the gap between VIPP1 spiral filaments. Two points on the spiral along the same radial direction with respect to the spiral center are indicated by r_1 and r_2 , respectively.

The filament thickness T is given by

$$T = r_2 - r_1 = r_0 \exp(k\theta) (\exp(2\pi k) - 1)$$
.

Meanwhile, the contour length S of the filament from the spiral center to r_1 is given by

$$S = \int_0^{\theta} r d\theta = \frac{r_0}{k} \exp(k\theta) - \frac{r_0}{k}.$$

Thus, T is linearly correlated with S,

$$S = \frac{T}{k(\exp(2\pi k) - 1)} - \frac{r_0}{k}.$$

Approximating lateral and longitudinal polymerization reactions as first-order reactions we have that

$$\frac{\partial T}{\partial t} = Pk_{\perp} ,$$

$$\frac{\partial S}{\partial t} = Pk_{\parallel} ,$$

where P is the concentration of freely-diffusing protein subunits in solution and k_{\perp} and k_{\parallel} are the lateral and longitudinal reaction rate constants, respectively. The ratio of k_{\perp} and k_{\parallel} is thus given by

$$\frac{\partial T}{\partial S} = \frac{k_{\perp}}{k_{\parallel}} = k(\exp(2\pi k) - 1).$$

Pan et al., 2024 Page 5 of 11

As a result, a logarithmic spiral could be formed by two first-order polymerization reactions in the lateral and longitudinal directions. Intuitively, the distal end of the filament exists for longer than the nascent filaments so that more subunits would bind laterally at the distal end.

VIPP1 dynamic logarithmic spiral model

During VIPP1 spiral growth, the VIPP1 spiral becomes larger, and we found that the distal tail rotated clockwise. To understand this dynamic process, we simulated three distinct kinds of spiral growth: (i) Archimedean spiral growth (**Supplementary Figure 4a**), (ii) logarithmic spiral growth (**Supplementary Figure 4c**). In these simulations, the arc length *S* increased at a constant rate with respect to time *t*, representing a constant longitudinal growth rate. By choosing the time unit as the reciprocal of the longitudinal binding rate, the simulation time step is unitary. The angular velocity of the filament end displacement is calculated from the displacement of the filament end projected on the tangent vector divided by the radius.

Archimedean spiral:

The spiral was simulated by $r = r_0 \theta$,

where $\theta = \sqrt{2S/r_0}$.

Logarithmic spiral:

The spiral was simulated by $r = r_0 \exp(k\theta)$,

where $\theta = \ln(kS/r_0 + 1)/k$.

Dynamic logarithmic spiral:

The spiral was simulated by $r = r_0 \exp(k\theta)$,

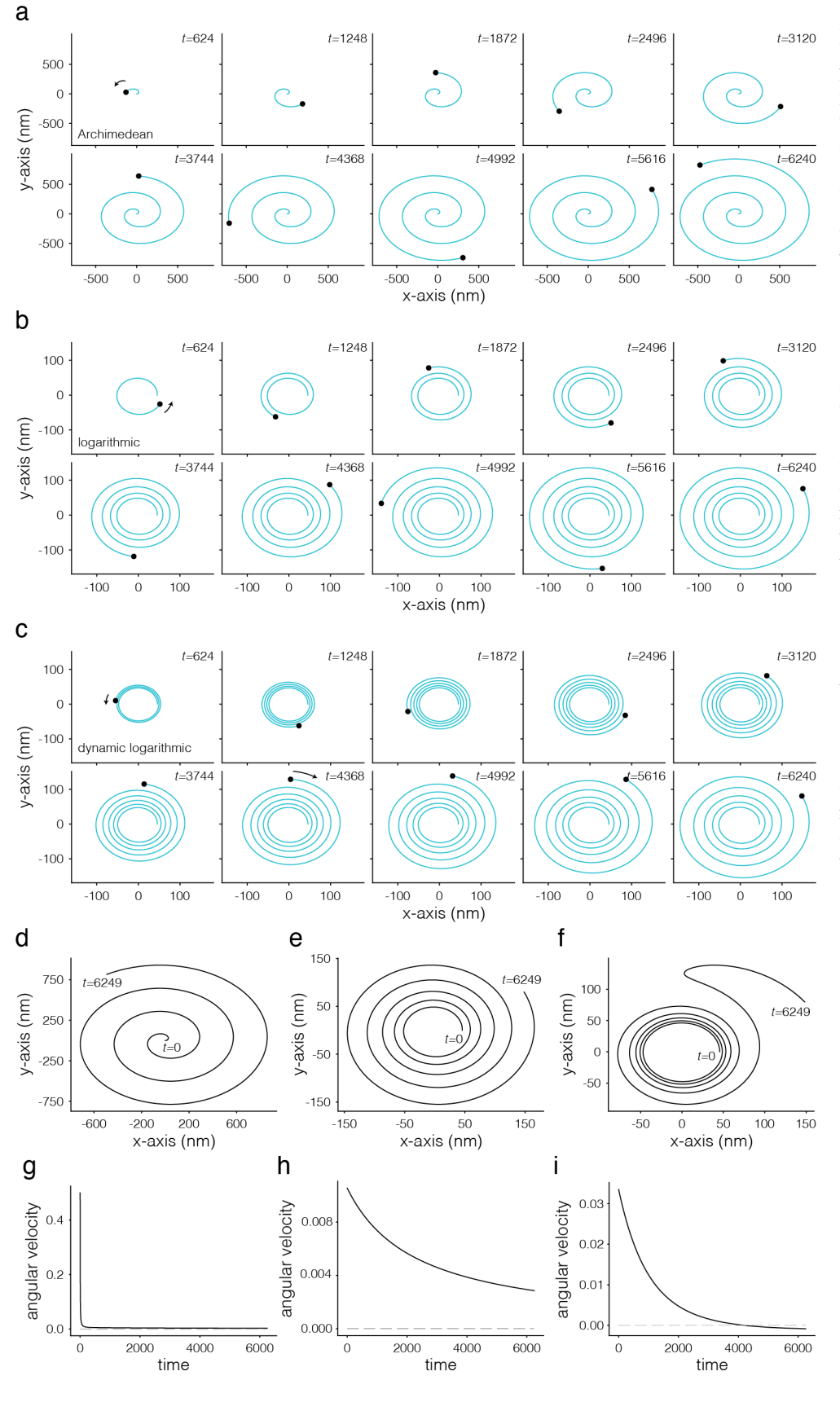
where k increases linearly over time t with slope s and intercept k_0 ,

$$k = k_0 + s \cdot t$$

while θ is calculated as for the logarithmic spiral.

In Archimedean (Supplementary Figure 4d) and logarithmic (Supplementary Figure 4e) spiral simulations, the filament end (black circle) always moves counterclockwise. In contrast, in the dynamic logarithmic spiral simulation, the filament end moves counterclockwise initially and then changes direction to move clockwise (Supplementary Figure 4f). The filament end angular velocities of the three kinds of spirals decay over time but only that of the dynamic logarithmic spiral changes direction (Supplementary Figure 4g-i) as observed in our experiments (Supplementary Movies 1 and 14). These simulation results support the conclusion that VIPP1 spirals mature from Archimedean spirals to (dynamic) logarithmic spirals through lateral annealing, especially at the more distal filament turns, which eventually leads to the clockwise rotation of VIPP1 spiral ends.

Pan et al., 2024 Page 6 of 11



Supplementary Figure 4 Filament growth simulations of Archimedean spirals, logarithmic spirals, and dynamic **logarithmic spirals.** The filament growth of (a) Archimedean spirals, (b) logarithmic spirals, and (c) dynamic logarithmic spirals was simulated as a function of time t. The filament ends are indicated by black dots. The growth direction is indicated by arrows. (d, e) The filament ends of Archimedean and logarithmic spirals form canonical spiral trajectories, representing a counterclockwise movement. (f) The filament end of a dynamic logarithmic spiral can form a noncanonical spiral trajectory, with a change in the direction of movement from counterclockwise to clockwise. Time stamps of trajectory start- and end-points are shown in each panel in (d,e,f). (g, h) The angular velocity of filament ends of Archimedean and logarithmic spirals decays over time but is always positive. (i) The angular velocity of the filament end of a dynamic logarithmic spiral decays over time before changing sign from positive to negative. The horizontal grey dashed line represents zero angular velocity.

Pan et al., 2024 Page 7 of 11

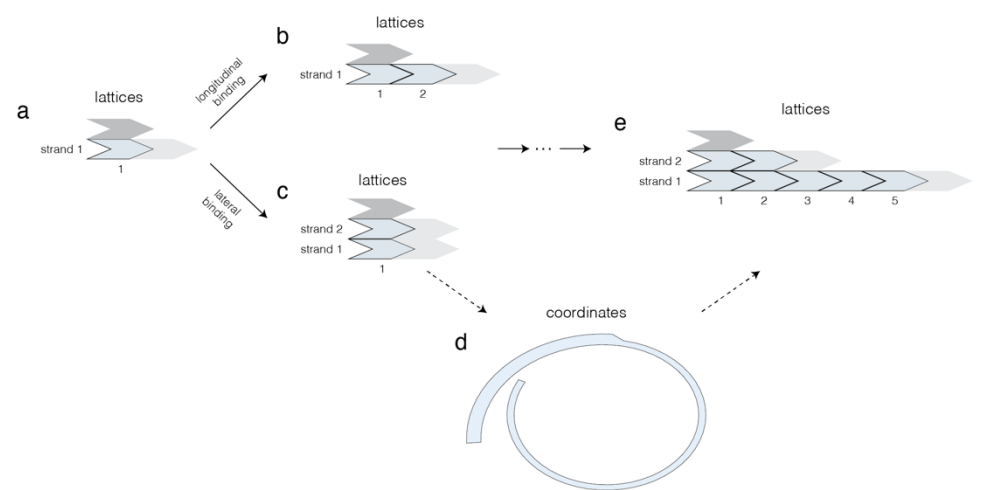
Supplementary Note 3: Monte Carlo simulation

Simulation procedure

To simulate the VIPP1 polymerization process by Monte Carlo methods, we used a coarse-grained model in which the filament was made up of multiple strands so that the binding/unbinding reactions on each lattice site (lateral interaction) could be simulated. As shown above (Supplementary Note 2) a dynamic logarithmic spiral growth process is needed to explain the clockwise propagation of the filament distal end in large spirals. In addition, as illustrated in Figure 5e in the main text (see also Supplementary Movie 14, top left), when filament growth was stopped upon meeting an obstacle, lateral annealing continued to thicken the filament in the strand located counterclockwise from the obstacle but did not propagate into the filament located clockwise from the obstacle.

The simulation was initialized from the nucleation site which was occupied by one subunit with intrinsic curvature c_0 (**Supplementary Figure 5a**). The following subunit binding could be lateral or longitudinal with binding rates r_{\perp}^+ or r_{\parallel}^+ , respectively. These binding reactions would thicken or elongate the filament, respectively. Meanwhile, the subunit unbinding from the tip of strands could be simulated with the longitudinal unbinding rate r_{\parallel}^- . The lateral unbinding rate between strands was ignored because the longitudinal unbinding of the last subunit in a strand is equivalent to the lateral unbinding to the strand below. The instantaneous binding/unbinding rates were calculated from the energy difference of the filament before and after the reaction event, as explained below. The reaction type and waiting time to the next step were determined by the Gillespie algorithm which considers the reaction rates of all possible reactions. If the reaction at the next step is a binding reaction, there are two possible filament configurations to consider: If subunit binding to the nucleation site is longitudinal, then the filament strand elongates by the length of a single subunit (**Supplementary Figure 5b**), while if subunit binding to the nucleation site is lateral, a new strand is introduced, which leads to a thickening of the filament by the width of a single subunit (**Supplementary Figure 5c**). If the reaction at the next step is unbinding, the subunit unbinds from the tip of the strand and the filament configuration is updated accordingly.

Consequently, the curvature of each lattice site was determined by averaging the local curvatures over 7 neighboring subunits, where the local curvature was obtained from the thickness of the filament according to the logarithmic spiral model in Extend Data Figure 3. Therefore, the coordinates of the filament could be generated from the strand count along the filament (**Supplementary Figure 5d**). Thus, the filament energy composed of the filament bending energy, as well as a Lennard-Jones potential energy, could be calculated to obtain reaction rates. Finally, after multiple simulation steps, we obtain the trajectories of the simulated growing spiral.



Supplementary Figure 5 | Monte Carlo simulation of VIPP1 filament growth. (a) The nucleation site was occupied by one VIPP1 subunit (light blue) following two possible binding pathways including lateral binding (dark gray) and longitudinal binding

Pan et al., 2024 Page 8 of 11

(light gray). (b) The new filament configuration generated from longitudinal binding. Longitudinal binding could continue on the tip of strand 1 or a subunit could bind to the nucleation site laterally. (c) The new filament configuration generated from lateral binding, which would introduce a new strand (strand 2) to the filament. Longitudinal binding could occur at the tips of all strands. (d) The coordinates of the simulated spiral were generated from the filament configuration. The coordinates were used to calculate the filament energy, which was used to calculate reaction rates at each simulation step. (e) After multiple simulation steps, a filament of different thickness and length composed of multiple strands is obtained.

Energy calculation

The total filament energy E is the sum of the filament bending energy E_{bend} and the Lennard-Jones potential energy E_{LJ} at all occupied lattice sites:

$$E = \sum_{\text{lattice}} E_{\text{bend}} + E_{\text{LJ}}.$$

Here, the bending of filaments contributes to E_{bend} and E_{LJ} was applied to model volume exclusion among filaments. Thus, if the filament was too strongly bent or was too close to another filament, the longitudinal unbinding rate r_{\parallel}^- would increase dramatically to counterbalance the filament energy.

Bending energy:

We assumed a single subunit was an elastic rod in which the bending energy $E_{\text{bend}}^{\text{subunit}}$ was a function of its curvature:

$$E_{\text{bend}}^{\text{subunit}} = \frac{1}{2} \kappa l (c - c_0)^2 ,$$

$$\kappa = Yhw^3/12 ,$$

where κ is the bending rigidity of the strand, Y is the Young's modulus of the filaments in the plane, l, w, and h are the length, the width, and the height of the subunit, respectively, and c and c_0 are the instantaneous and intrinsic curvatures of the strand, respectively.

Because the filament comprised multiple strands, the curvatures of subunits on the same lattice were slightly different (**Supplementary Figure 6a**). The curvature c_i and the length l_i of subunits in strand i were calculated according to the geometric relationship:

$$c_i = (c^{-1} + w(i - 1 - (n - 1)/2))^{-1},$$

 $l_i = \frac{lc}{c_i},$

where c is the curvature of the neutral axis of the filament on the lattice, and n is the total number of strands on the lattice. Therefore, the bending energy on an individual lattice, E_{bend} , was the sum of E_{bend} of all subunits on that lattice:

$$E_{\text{bend}} = \sum_{i=1}^{n} E_{\text{bend}}^{i} = \frac{1}{2} \kappa \sum_{i=1}^{n} l_{i} (c_{i} - c_{0})^{2}.$$

Lennard-Jones potential:

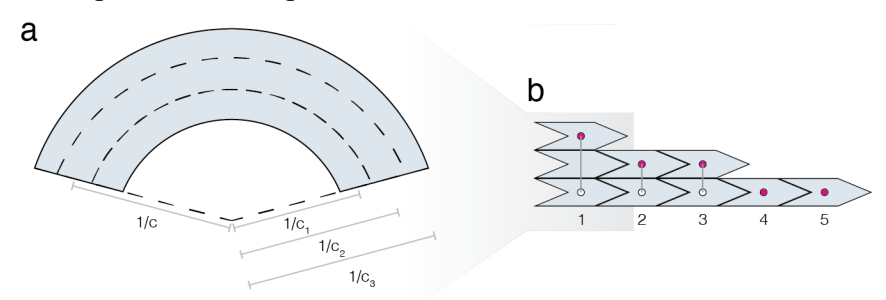
Volume exclusion effects among filaments was modeled via a Lennard-Jones potential, which can be evaluated as the sum of potentials of each outermost subunit in the filament:

$$E_{\rm LJ} = \sum_{\rm lattice} \sum_{i} 4\epsilon \left(\left(\frac{\sigma}{d_i} \right)^{12} - \left(\frac{\sigma}{d_j} \right)^{6} \right)$$

where ϵ is the interaction strength, σ is the contact distance between subunits, and d_j is the distance from a given outermost subunit to the line segment connecting the outermost and innermost subunits on the *j*th lattice

Pan et al., 2024 Page 9 of 11

(Supplementary Figure 6b). The potential was set to zero for separations greater than the cutoff distance $d_c = 1.12\sigma$, which is the separation at the potential minimum.



Supplementary Figure 6 | **Calculating the energy of filament configurations.** (a) Three strands on a lattice, stretched to different lengths and with different curvatures. The schematic is exaggerated for illustration. (b) A filament composed of 3 strands and 5 lattices. The outermost and innermost subunit on each lattice is indicated by a red and white dot, respectively. The line segments connecting the outermost and innermost subunits are indicated by gray lines. The subunits on the first lattice are enlarged in (a).

Calculating the rates of binding and unbinding

Because the total concentration of VIPP1 in solution, \bar{C} , was of great excess, we treated \bar{C} as being constant. We also assumed the binding was diffusion-controlled, so that the binding rates were determined by the product of VIPP1 concentration and the lateral binding rate constant k_{\perp}^+ or the longitudinal binding rate constant k_{\parallel}^+ , respectively. When an additional subunit laterally associates to the nucleation site, the local curvature is lower than the intrinsic curvature c_0 of the initial subunit, leading to an increase in bending energy $E_{\rm bend}$. We assumed that lateral binding was favored when the subunit curvature was close to the strand curvature. Therefore, the apparent lateral binding rate r_{\perp}^+ was calculated from a Boltzmann distribution of subunits with curvature close to the intrinsic curvature:

$$r_{\perp}^{+} = k_{\perp}^{+} \cdot \bar{C} \cdot \frac{\exp(-\beta E_{\text{bend}})}{Z},$$

with $\beta=(k_BT)^{-1}$ is the inverse thermal energy and Z is the partition function. We set \mathcal{L}_{\perp}^+ as a constant parameter in the simulation $\mathcal{L}_{\perp}^+=k_{\perp}^+\bar{C}/Z$, because subunits in the initial lateral binding adopt the preferred curvature. Similarly, the initial longitudinal binding rate $\mathcal{L}_{\parallel}^+=\mathcal{L}_{\parallel}^+=k_{\parallel}^+$ was another constant parameter and the instantaneous longitudinal unbinding rate $\mathcal{L}_{\parallel}^-$ was calculated from the expression

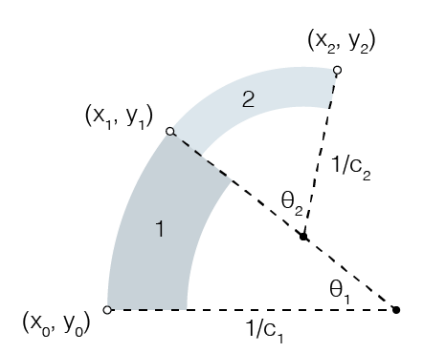
$$r_{\parallel}^- = r_{\parallel}^+ \cdot \exp(-\beta(\Delta E + \mathcal{E}_{adh}))$$
,

where \mathcal{E}_{adh} is the adhesion energy of a single subunit bound to the filament and ΔE is the total energy difference between the filament states before and after the subunit unbinding. The total energy of the filament was obtained by adding the bending energy and the Lennard-Jones potential energy, as described above.

Generation of spiral coordinates

A spiral shows different curvatures along the filament. We employed the logarithmic spiral model, as depicted in main text Figure 5 and Extended Data Figure 3, to establish the correlation between radius and thickness. Once the radius of curvature of each lattice (labeled 1 and 2 in **Supplementary Figure 7**) was determined, the coordinates of the spiral could be generated by rotating the angle θ_i , which was determined by the curvature and the arc length of lattice i. The curvature of each lattice was used to calculate the bending energy of the filament and the coordinates of the spiral were used to calculate the Lennard-Jones potential energy.

Pan et al., 2024 Page 10 of 11



Supplementary Figure 7 | Generation of spiral coordinates from filaments. The coordinates of the adjacent lattice (x_2, y_2) were generated based on the coordinates of the previous lattice (x_1, y_1) by rotation of a specific angle θ_2 , which was determined from the curvature.

Supplementary Table 1. Simulation parameters

Parameter	Symbol	Value	Estimated from
Intrinsic curvature	c_0	0.077 nm ⁻¹	Figure 2b
Arc length of subunit	ℓ	4.8 nm	Figure 2g and Figure 3h
Width of subunit	w	5 nm	Figure 4g and Figure 5e
Height of subunit	h	7.2 nm	Figure 1i
Young's modulus	Y	34 kPa	Figure 2e
Lennard-Jones interaction strength	ϵ	$2 k_B T$	Pfitzner et al., 2020
Lennard-Jones contact distance	σ	5 nm	Same as width of subunit
Initial lateral binding rate	\mathscr{V}_{\perp}^{+}	0.1 s^{-1}	Figure 4f
Longitudinal binding rate	r_{\parallel}^{+}	6 s ⁻¹	Figure 4g
Adhesion energy	$\mathcal{E}_{ ext{adh}}$	$3 k_B T$	Adjusted to fit result in Figure 4b

Pan et al., 2024 Page 11 of 11